UNIVERSITY OF CALIFORNIA
RIVERSIDE

Scanning Tunneling Microscopy Study of Molybdenum Disulfide and Its Derivatives on Cu(111)

A Dissertation submitted in partial satisfaction
of the requirements for the degree of

Doctor of Philosophy

in

Chemistry

by

Wenhao Lu

August 2014

Dissertation Committee:
Dr. Ludwig Bartels, Chairperson
Dr. Yadong Yin
Dr. Robert C. Haddon

The Dissertation of Wenhao Lu is approved:

_____

_____

_____

Committee Chairperson

University of California, Riverside

Acknowledgements

Firstly, I would like to thank my research advisor, Ludwig Bartels, for a lot of reasons. I want to thank him for providing me with this great opportunity to study and do research in his lab, and for supporting me as a research assistant through last five years. Moreover, I want to thank him for his guidance and advices. Whenever I got lost in a research project or I was confused about any experimental results, Dr. Bartels was always able to tackle the problem quickly and put me back onto the track. He is knowledgeable in physics, chemistry, electronic engineering and material sciences, which helped me investigate many novel phenomena we observed in our experiments and his experienced and creative thoughts helped me gain more insights.

Secondly, I would like to thank Professor Robert C. Haddon and Professor Yadong Yin for serving on both of my advancement to PH.D. candidate and doctoral committees.

I would like to thank the following previous group members who also taught me a lot of STM techniques or worked with me : Dr. Dezheng Sun, Dr. Daeho Kim, Dr. Miaomiao Luo, Dr. Yeming Zhu, Dr. Zhihai Cheng, Dr.Greg Pawin, Dr.Jon Wyrick, Dr. John Mann, as well as current group members: Chen Wang, Quan Ma, Sarah Bobek, John Mann, Edwin Preciado, KatieMarie Magnone, Jessica McKinley, Velveth Klee, Miguel Isarraraz, Michael Gomez, Koichi Yamaguchi. et. al. Especially, I would like to thank Chen Wang who has worked with me on the current STM for 3 years and helped me a lot for

modeling analysis and theoretical calculation. I also want to thank Quan Ma who helped me a lot for equipment design and optimization on STM. I have learned many useful techniques and skills from my group members. I am also very pleased to see more and more talented students are joining our group.

I also would like to thank Dr. Duy Le from Talat Rahman's group, Prof. Talat Rahman and Prof. Theodore L. Einstein, who collaborated with us and provided us a lot of supporting of theoretical calculations.

Finally, I would like to thank my Parents for bringing me to this world, for all of the sacrifices that they have made for me, for all that they have been doing in order to make me a better life. Besides, I would like to thank all my friends at Riverside who supported me whenever I had tough time during graduate study.

ABSTRACT OF THE DISSERTATION

Scanning Tunneling Microscopy Study of
Molybdenum Disulfide and Its Derivatives on Cu(111)

by
Wenhao Lu

Doctor of Philosophy, Graduate Program in Chemistry
University of California, Riverside, August 2014
Dr. Ludwig Bartels, Chairperson

The Scanning Tunneling Microscope (STM) is well known as one of the best spatially resolved microscopes today. Due not only to its microscopic ability, but also to its capability to manipulate individual atoms or molecules, it has been used as a very powerful tool in furthering the miniaturization of nanodevices. In my thesis, molybdenum disulfide(MoS_2) and its derivatives on Cu(111) at low temperature in ultra-high vacuum(UHV) conditions are systematically investigated using a home-built STM. By slightly changing the preparation methods, we can synthesize MoS_2 monolayers, Mo_2S_3 monolayers or Mo_6S_6 nanowires. Density Functional Theory (DFT) calculations were also performed to support and interpret experimental results.

TABLE OF CONTENTS

List of Figures

List of Tables

Chapter 1 Introduction

1.1 Scanning Tunneling Microscopy

The invention of the Scanning Tunneling Microscope (STM) by Gerd Binnig and Heinrich Rohrer in 1981 opened a new world to the field of microscopy. [5] STM has not only been used to produce images of metallic and semiconducting surfaces with unprecedented spatial resolution [5, 6], it has also been used to manipulate individual atoms and molecules. [7] Also, by adding ultra-high-vacuum and low-temperature features, site-specific vibrational spectroscopy of adsorbates was made possible.

The principle of STM is based on tunneling, which is a quantum mechanical phenomenon. In classical mechanics, an electron traveling between the sample and the tip would require an energy greater than the work function of tip/sample material to overcome the energy barrier between them. [8] However, in quantum mechanics, the electrons are able to tunnel through the barrier with a certain probability. If an electron is put into a one-dimensional junction with a rectangular barrier, its state would be:

$$\Psi(z) = \Psi(0)e^{-kz}$$

where

$$k = \frac{\sqrt{2m_e(U - E)}}{\hbar}$$

ψ is the electronic wavefunction, z is the tip-sample separation, m is the electron mass,

U is the potential in the barrier, E is the energy of the tunneling electron, and ħ is Planck's constant.

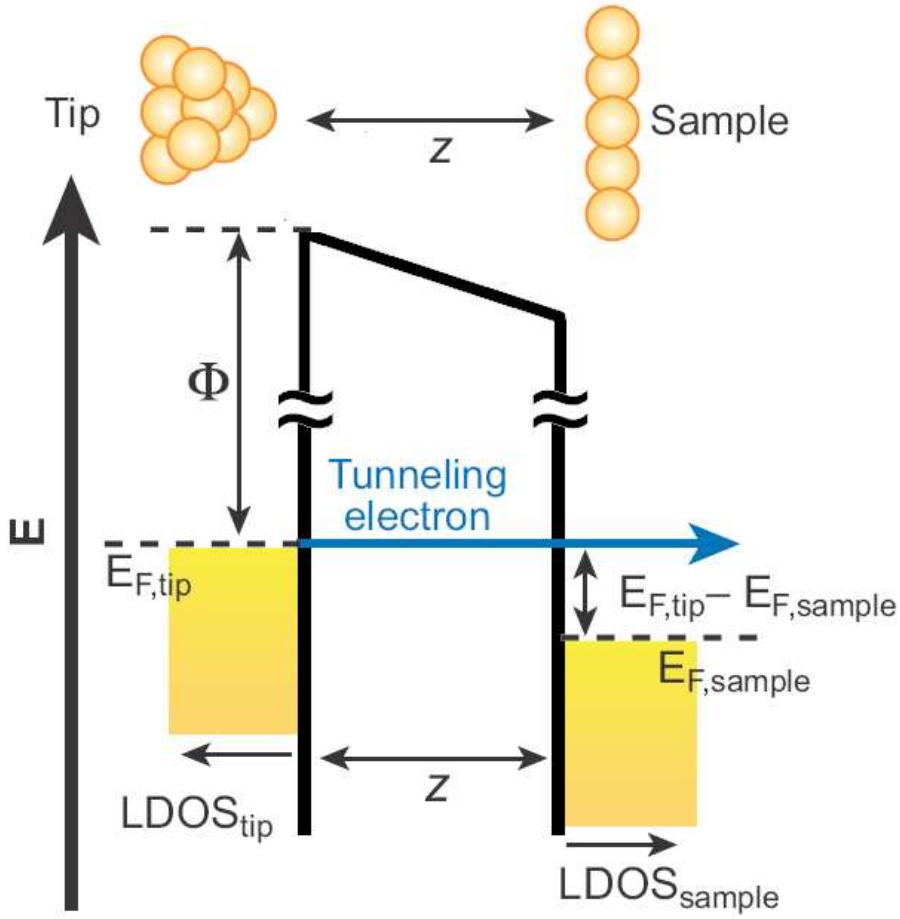

Fig 1.1 An energy level diagram for a one dimensional electron-tunneling junction. The Fermi energy levels (E_F) of the tip and sample are offset by the applied bias voltage (V) times the electron charge (e). The resultant current is exponentially dependent on the distance between the sample and the tip (z). LDOS, local density of states; Φ, work function of the metal

By the Born interpretation of the wavefunction, the square of the wavefunction is proportional to the probability distribution of the electron, and thus, the probability of tunneling yielding a tunneling current I:

$$\Psi(z)^2 \propto e^{-kz} \propto I(z)$$

The molecular and atomic resolution of STM is enabled through this exponential current decay. Therefore, the tunneling current is extremely localized, and the STM is sensitive to both lateral and vertical changes in topography (often tenths of angstroms or less).[9, 10]

The sensitive dependence of the tunneling current on the tip-sample distance is not the whole story of how the atomic resolution of the STM is achieved. In reality, in order to reach such a precise control of the displacement and motions of the tip and sample, it is necessary to manipulate the sample or tip by using piezoelectric materials. Piezoelectric materials respond to an applied electrical voltage with a mechanical deformation. For example, Quartz is a commonly used single crystalline piezoelectric material. Some polycrystalline ceramics also exhibit piezoelectricity, and can be produced through a polarization process in a strong electric field.[11] Lead zirconium titanate (PZT) ceramics are typically used in scanning probe microscopes, with a 10pm to 1Å resolution at a typical dimension.

In order to maintain a stable tunneling junction between the tip and sample, the system must be separated from any noise, including the noise both inside and outside of STM. STM systems are mounted on air tables that isolate them from ground vibrations. Besides, both the STM and controller should be grounded. This is important to obtain an undisturbed image, excluding both physical vibration and electronic noise.

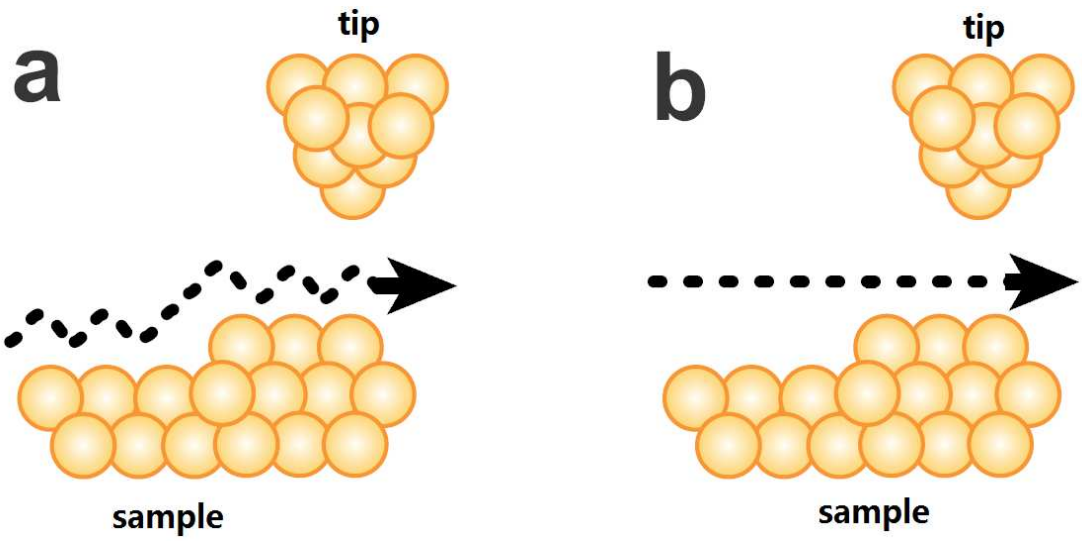

Fig 1.2 (a)Schematic of a scanning tunneling microscopy (STM) tip scanning across a metal surface in constant-current mode. The tip is extended and retracted, maintaining a constant tunneling current between tip and sample. (b) Schematic of a STM tip scanning across a metal surface in constant-height mode, maintaining a constant tip-sample separation, measuring current.

The STM tip is scanned across a surface mostly in two different modes: constant current (Fig 1.2a) or constant height (Fig 1.2b). The constant-current mode is the most common mode, the feedback loop (FBL) maintains a set current by adjusting the tip-sample separation. The topography is recorded and it depends on both the geometric structure and the local density of states (LDOS) of the tip and sample [3, 12]. Constant current mode is able to measure surface features with higher precision as described above, but is generally slower due to the need for mechanical manipulation of the scanner in the z direction, controlled through the FBL. In constant-height mode, the tip is maintained at a set distance from the sample during scanning, recording the current and allowing for much faster measurements; constant-height mode is most useful for relatively smooth surfaces.

1.2 STM Specifics

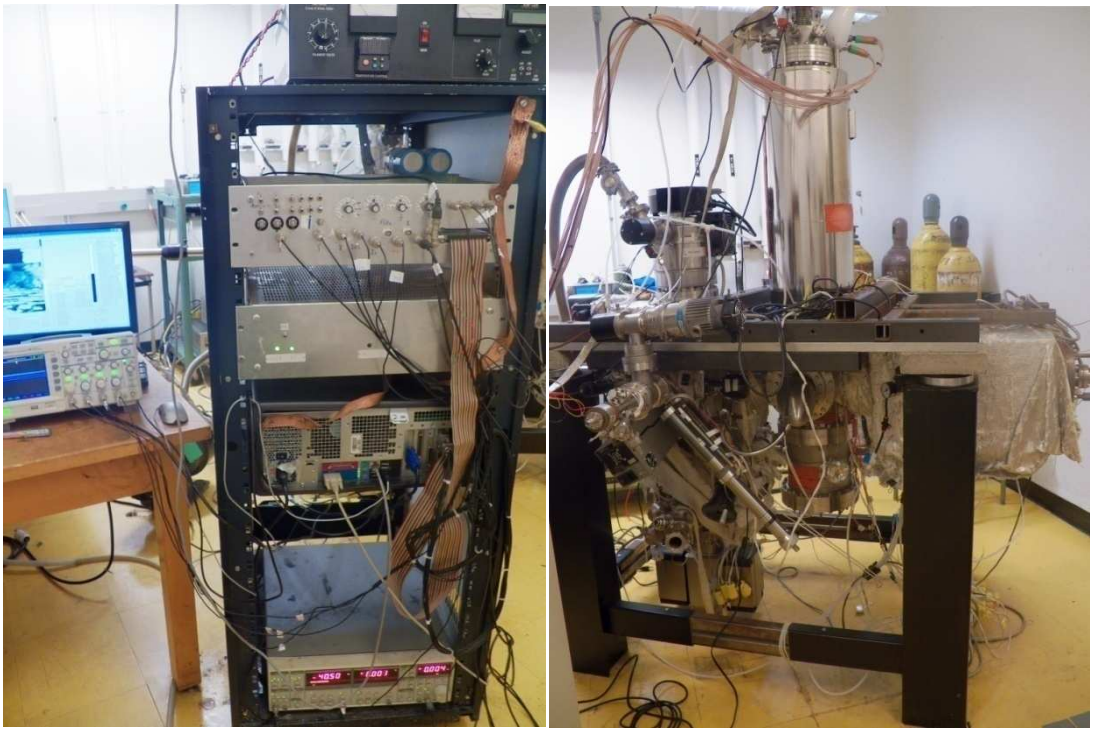

Fig 1.3 Home-built ultra high vacuum (UHV) STMs in Bartels group with control system (left) and cooling systems of bath cryostat (right).

Three STM systems were used to perform the experiments in Bartels group. For this study, the STM used is illustrated in Fig 1.3. This STM is equipped with a bath cryostat which has better vibration isolation than continuous flow cryostat due to the absence of a cryogenic liquid (Liquid N_2 or Liquid He) transfer line from the dewar and noise of flow. This system can be cooled to ~78K with Liquid Nitrogen and ~10K with Liquid Helium.

This STM system has an UHV chamber split into two parts: preparation chamber and scanning chamber. Preparation chamber functions as a sample preparation area

with a sputter gun, molecule dosing setup, e-beam evaporator, thermo couple, mass spectrometer, turbo pump and ion pump. Scanning chamber consists of wobble stick access to the cryostat door and STM spring mechanisms, ion pump, titanium sublimation pump (TSP) and the scanning core unit of STM.

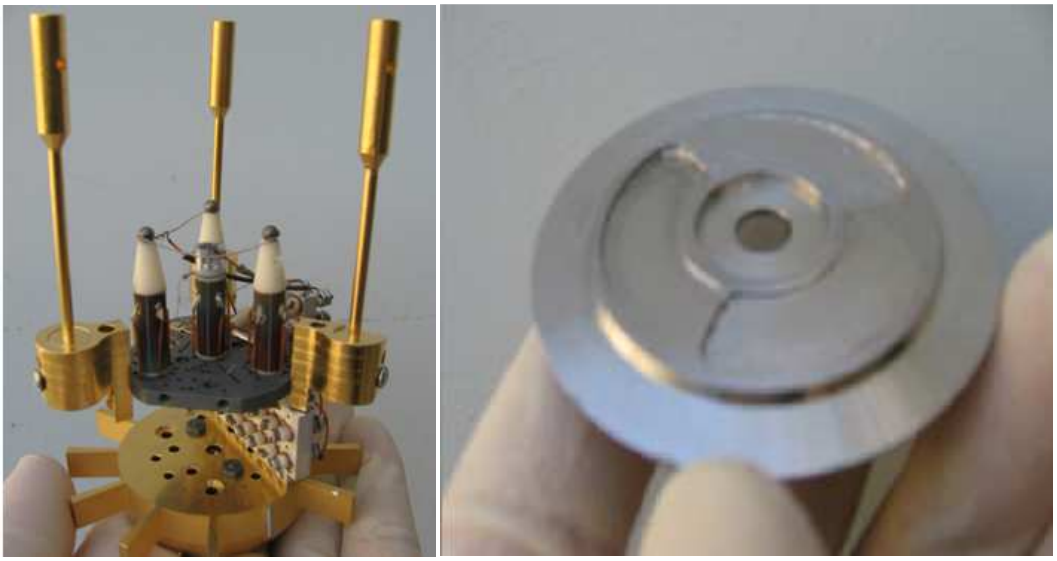

Fig 1.4 Scanning unit(left) and a ramp(right) of the scanning tunneling microscope I have been working on.

Fig 1.4 shows a scanning core unit and a ramp. There are three outer piezoelectric tubes for the movements of the x and y axes and one central piezo for the fine z-axis movement. On the top of each outer piezoelectric tube, a well polished metal ball is positioned to give slip-stick motions to the ramp so that it can move vertically. On the top of the center piezoelectric tube, the tungsten tip is positioned upside down. While scanning, the ramp is positioned onto the piezoelectric tubes and three outer piezoelectric tubes give x- and y-axis movements, and the center piezoelectric tube

independently moves only in the z-axis to continuously be adjusted to maintain a constant tunneling current.

It is very important to isolate the vibrations from the ground during STM measurement. For this purpose the tables of the whole system is floated with high-pressure gas (30psi in use). Turbo pumps are used during the sample preparation process to provide UHV, but they will be stopped during STM measurement to avoid vibrations and all the cables are detached to the chambers except the necessary ones for signal transferring.

1.3 Experimental Procedure

Preparation of the sample typically consists of two parts: substrate cleaning and MoS_x preparation. In certain cases, molecule/atom are deposited onto MoS_x to characterize the chemical or physical properties of different MoS_x structures.

1.3.1 Cu(111) Substrate Preparation

In this study, a Cu(111) single crystal is used as the substrate. A Cu(111) crystal has a face-centered-cubic(fcc) unit cell with a lattice constant of 2.55Å. For fcc Cu(111) surface, the step edges are parallel to each other or form 60°. Clean (111) surface is provided for further growth of MoS_x structures.

A dirty and rugged Cu surface is shown in the left of Fig 1.5. To provide smooth and clean surface, the crystal was cleaned by cycles of sputtering and annealing. Before each sputtering, a Titanium sublimation pump was run for ~3 minutes to improve the vacuum. During sputtering, thermal electrons are produced with 20mA of filament emission current and accelerated by 3kV electric field, which further ionize Ar to Ar^{+} at $2x10^{-5}$torr of Ar gas pressure. For annealing, a coil of tungsten wire, 0.006" in diameter, and of approximately 6cm in length, was used as a radiation heating method. With this filament, a total power of ~22W was set with ~1.2A of current and ~18V of voltage and the sample was annealed for 20 minutes. Using this setup, the temperature of the Cu(111) single crystal sample can be heated up to 500°C, at which point copper begins to glow. At this temperature, surface melting can occur and surface copper atoms rearrange to form large terraces. After six or more sputtering and annealing cycles, the cleanliness of the sample was confirmed by STM scanning at room temperature and liquid nitrogen temperature (~78K). Fig 1.5 shows an STM image of a clean Cu(111) single crystal terraces.

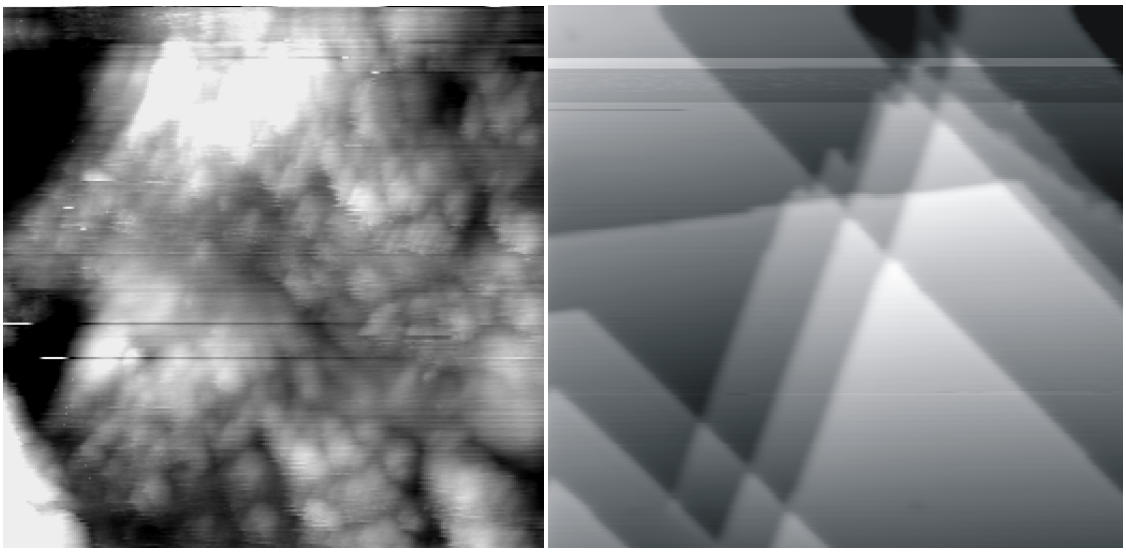

Fig 1.5 A dirty Cu surface(left) and a clean Cu(111) surface (52nm × 52nm) with copper step edges which are parallel to each other or form 60 degrees(right) .[2]

1.3.2 Molecule Deposition

The deposition methods are slightly different for molecules with various vapor pressures. Molecules with low vapor pressure, smaller than 10^{-9} torr at room temperature, are typically in the solid phase. Heating is required to sublime the molecule to the metal substrate. The sample is aligned in a line-of-sight fashion with the molecule source in a glass capillary, to collect the beam of moving molecules more efficiently. It is noted that pretreatment of degasing is required to get rid of impurities with lower vapor pressures. This is generally achieved by preheating the glass capillary with a slightly higher temperature than that for sublimating the substrate.

For molecules with higher vapor pressure, mostly larger than 10^{-9} torr, heating is unnecessary. Instead a leak valve is required to control the amount of molecules leaking into the chamber. Freeze-pump-thaw cycles are needed to purify liquid samples, because quite a large amount of gases from the air could be dissolved in liquids. The procedures are- as indicated in the notation- first freezing the liquid (generally with a cooling bath of liquid nitrogen), followed by applying a vacuum condition, then thawing the molecules in a warm water bath to release the trapped gases as bubbles. Several cycles are required until no bubble is seen during thawing. Further checking the purity of the sample with mass spectrometer is always necessary.

For both of the solid sample and liquid sample, the pressure needed for dosing depends on the vapor pressure of the sample and can be further calibrated with mass spectrometer when compared to other peaks (i.e. N_2). Besides, the dosing time depends on how much molecules needed for the specific experiments.

1.3.3 Metal Deposition

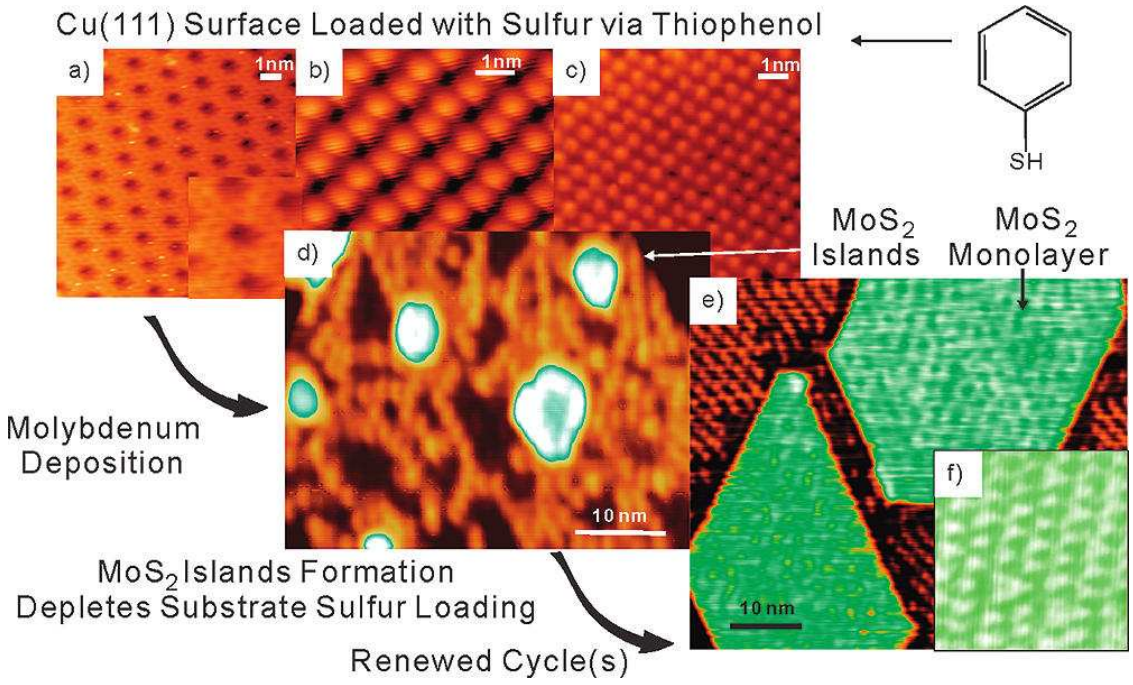

Fig 1.6 Preparation of (d) MoS_2 monolayer islands and (e) larger flakes on a Cu(111) surface through (a–c) initial loading of the substrate with sulfur via (top right) thiophenol exposure. The resultant MoS2 monolayer is highly ordered and oriented in the same crystallographic direction across all islands on the surface. Image parameters: (a) bias, −130 mV; current, 50 pA; (b) bias, −250 mV; current, 60 pA; (c) bias, −2.2 V, current, 60 pA; (d) bias, −170 mV; current, 80 pA; (e) bias, −2.1 V; current, 140 pA; (f) bias, −110 mV; current, 150 pA. [4]

In order to deposit metals such as molybdenum or copper, a metal evaporator is installed onto the preparation chamber. In general, there are two types of metal evaporators differing in their heating mechanisms: thermal heating and e-beam heating. For thermal heating, the metal source, either a pellet or rod is in contact with a heating filament. Thermal conduction heats the metal and a flux of metal beam is generated. In the e-beam heating, a filament is heated to generate hot electrons which are then accelerated to the metal source by applying a positive high voltage (3kV in this project).

The advantage of using e-beam heating is it can generate much more power on the source, which allows depositing high melting point material like tungsten and molybdenum. Normally a flux monitor attached to the evaporator checks the deposition rate. When used in combination with a quartz crystal thickness monitor, a precisely controlled deposition can be achieved.

1.3.4 MoS_x Preparation

For preparing MoS_2 on Cu(111) substrate, here is an overview of the method [4]: initially, a copper surface is prepared that is dominantly covered with sulfur through exposure to thiophenol at ~100 K and 10^{-7} Torr (as measured with an ion gauge using a N_2 calibration factor) for 300–400 s (i.e., for a dose of ~30–40 Langmuir. In this case, thiophenol is overdosed), followed by annealing to 400–500 K. This leads to the formation of various sulfur superstructures (Fig 1.6 a–c) coexisting on the substrate. The subsequent deposition of molybdenum by e-beam evaporation leads upon annealing at ~500 K for 20 min to the formation of MoS_2 hexagons and triangles of a few nanometer in size while at the same time depleting the surface sulfur loading. The repeated application of thiophenol and exposure to molybdenum allows the successive growth of large monolayer flakes.

An improved and simplified preparation method of MoS_2 is as follows: a highly dense sulfur terminated copper is prepared by dosing thiophenol to clean Cu(111) sample at a pressure of 2×10^{-7} Torr for 300 s (i.e., for a dose of ~60 Langmuir. In this

case, thiophenol is overdosed), followed by annealing to 400–500 K. Then, keep dosing thiophenol to clean Cu(111) sample at a pressure of 6×10^{-8} Torr for 600 s, meanwhile, annealing the sample to a temperature of ~400K. The subsequent deposition of molybdenum by e-beam evaporation and dosing thiophenol with a low pressure of 3×10^{-9} torr leads upon annealing at ~500 K for 20 min to the formation of MoS_2. In this case, the repetition of dosing thiophenol and molybdenum can be simplified.

The preparation of molybdenum sulfide derivatives like Mo_2S_3 and Mo_6S_6 is almost the same as preparing regular molybdenum disulfide except the annealing temperature and the pressure of thiophenol when dosing molybdenum are both lower. After preparation, Mo_6S_6 can be restructured into MoS_2 with high temperature annealing (i.e. 600K), but Mo_2S_3 is still as stable as MoS_2 at high temperature

1.3.5 Density Functional Theory Simulations

In order to determine the electronic structure, molecular geometries, and binding energies of the species of interest at various adsites, we used Density functional theory (DFT) calculations. All DFT calculations were performed with the Vienna Ab Initio Simulation Package (VASP) [13] implementing the generalized gradient approximation (GGA) for the exchange-correlation functional [14] and the plane-wave pseudopotential method. [15] it is possible to get a better understanding of the fundamental interactions and processes taking place in these systems by combining the results of these

theoretical calculations with our experimental data. The detailed setup and results for each theoretical simulation will be addressed in the corresponding chapter.

We have our own computer sets for the theoretical calculations, meanwhile we also collaborate with Talat Rahman's group from University of Central Florida and Einstein group from University of Maryland for more support of theoretical calculations.

Chapter 2 Towards the Growth of an Aligned Single-Layer MoS_2 Film

The following is taken from an article I published in Langmuir: D. Kim, D. Sun, **W. Lu**, Z. Cheng, Y. Zhu, D. Le, T. S. Rahman, and L. Bartels, Toward the Growth of an Aligned Single-Layer MoS_2, Langmuir, 2011, 27 (18), pp 11650–11653. This was collaborative work reporting on measurements by me and other graduate student (D. Kim, D. Sun, Y. Zhu) and postdoctoral (Z. Cheng) members of the Bartels group on the STM I am working on. Computational support came from D. Le of the group of T.S. Rahman of the University of Central Florida.

2.1 Introduction

MoS_2 is a semiconducting material consisting of sulfur-molybenum-sulfur tripledecker layers loosely bound by van der Waals interactions. MoS_2 has been used technologically for a long time, for instance as dry lubricant employing its layered character similar to graphite. Recently, its electronic characteristics have attained increased attention with the finding that it transits from an indirect bandgap semiconductor at 1.6eV gap to a direct bandgap one at 1.9eV gap at the transition from multilayers to a single layer [16, 17]. A transistor with appreciable properties has been constructed from MoS_2 [18] and core shell particles have been prepared [19]. The

increased bandgap and high fluorescence yield at the monolayer limit may also suggest applications of the material for photonic or photocatalytic applications. Consequently, MoS_2 is seeing some interest as a natively semiconducting analogue of graphene [20].

MoS_2 can be exfoliated mechanically similar to graphene [21]. While this method is simple, it is hard to control and not amenable to mass production of thin films. Solution-based processes have been proposed and may provide a scalable source of a mixture of single and multilayer material [22]. Also ultra-high vacuum deposition of size-selected MoSx clusters has been achieved [23]. Here we propose an alternative avenue for the fabrication of MoS_2 monolayers: growth of MoS_2 on a sulfur-preloaded copper surface. In contrast to all other methods, this route has the potential of providing exclusively monolayer material, as the sulfur source is only available until the substrate is covered. Practically, this approach is related to the growth of graphene monolayers on copper [24] or iridium films [25], where segregation of carbon to the surface is employed in aggregating a carbonaceous layer that transforms into graphene under the correct conditions.

Small MoS_2 triangles of a few nanometers in size have been grown previously on gold in a dilute H_2S atmosphere [26] or other S precursors [27]. Here we show significantly larger patches, tens of nanometers in size whose crystallographic axes are aligned with that of the underlying substrate. In contrast to gold, copper forms a multitude of sulfur surface structures and also readily absorbs sulfur into the bulk

[28-34]. Thus, we can preload the substrate with a sufficient amount of sulfur using an easy to handle liquid precursor, thiophenol (benzenethiol).

In previous work we have shown that heating to ~400K removes the phenyl group of thiophenol reliably and cleanly from copper leaving a sulfur coverage behind. Here we observe published and several additional sulfur superstructures; following Molybdenum deposition, we witness the transfer of sulfur from the copper surface into thermodynamically more favorable MoS_2 islands.

2.2 Experimental Section

This study reports on a first step towards the formation of closed monolayer films. It was conducted within an UHV chamber equipped with an e-beam evaporator (Omicron) for Molybdenum deposition, leak valve for benzenethiol exposure, sample heater for annealing, mass spectrometer for vacuum analysis and a home-built low-temperature scanning tunneling microscopy (STM) setup for structural analysis of the resultant film. The metal evaporator is calibrated with a quartz crystal microbalance and the deposition rate is held stable via measurement of the ion flux. In a separate UHV system we conducted x-ray photoelectron spectroscopy (XPS) to ascertain formation of MoS_2. Sample preparation following sputter-anneal cleaning of a Cu(111) single crystal started by deposition of thiophenol, removal of the phenyl groups through annealing, subsequent deposition of Molybdenum and renewed annealing to form MoS_2. Between each step we surveyed the surface by STM at liquid nitrogen

temperatures. Although this study was conducted on a single-crystal substrate, single-cyrstallinity is clearly not a precondition for the applicability of the method, as any clean copper film is overwhelmingly covered with (111) facets.

2.3 Results and Discussions

Fig 1.4 shows an overview of the method: initially, a copper surface is prepared that is dominantly covered with sulfur through exposure to thiophenol at ~100 K and 10^{-7} torr (as measured with an ion gauge using N_2 calibration factor) for 300-400 s, i.e. for a dose of ~30-40 Langmuir, followed by annealing to 400-500 K. This leads to the formation of various sulfur superstructures (**Error! Reference source not found.**Fig 1.4 a-c) coexisting on the substrate. Subsequent deposition of Molybdenum by e-beam evaporation leads upon annealing to ~500 K for 20 min to the formation of MoS_2 hexagons and triangles of a few nanometer in size, while at the same time depleting the surface sulfur loading. Repeated application of thiophenol and exposure to Molybdenum allows the successive growth of large monolayer flakes.

Prior thermally programmed desorption experiments of thiophenol on Cu(111) showed that phenyl desorbs intact from the substrate predicting that there is no significant carbon contamination of the surface [35]. This allows the use of thiophenol as a sulfur source. Thiophenol is an easy to handle liquid, in contrast to H_2S gas used in most previous studies. From a practical perspective this has similar advantages as the use of TEOS (tetra-ethyl ortho-silane) over silane in chemical vapor deposition.

Exposure of a Cu(111) surface to thiophenol leads initially to the formation of the honeycomb structure (Fig 1.4a) with a larger (√43×√43) R 7.5°unit cell followed by a pattern of zigzag rows (Fig 1.4b) and a hexagonal structure (Fig 1.4c). Their sulfur surface content ranges from ~0.3 to ~0.4 sulfur atoms per surface copper atom [32, 34]. Each of these structures contain sulfur atoms in at least two different kinds of local geometries, with those coordinated near in-plane to four copper atoms commonly assigned as the protrusions in STM. In our study we observe most commonly the zigzag rows shown in Fig 1.4b, but also several other patterns (some of which are not shown and not described in the literature). Given that there has been some controversy about the precise atomic structure of these patterns, a more detailed discussion is beyond the scope of this manuscript [28-34].

Deposition of Molybdenum on the room-temperature sample followed by annealing (~500K) allows the formation of MoS_2 islands. While at a deposition flux in the Å/min range the formation of three-dimensional Molybdenum clusters on the surface dominates, at very low deposition flux (Å/h range) we find the formation of MoS_2 islands after annealing. In line with these findings, we observe reduction of the sulfur coverage on the surface only in the case of slow deposition (Fig 2.1). We also deposited Molybdenum onto the substrate at elevated temperatures, but substrate heating could not alleviate the need for very slow deposition rate to favor MoS_2 over Mo-island growth. Clearly, the interplay between Molybdenum Disulfide formation, diffusion of

Molybdenum, sulfur or any potential MoS_x species is a complex one; further efforts will attempt to find optimal parameters for flux and deposition rate.

The resultant MoS_2 islands are 3.2±0.1Å in height, as observed by STM. This is in good agreement with the distance between the top and bottom sulfur layer of 3.16Å in the bulk. Density functional theory simulation of the expected apparent height of MoS_2 on Cu(111) predict 4.0Å. The bond distance between inert species/layers and metallic surfaces is typically underestimated by DFT methods even including van der Waals interactions (for instance, benzene on Cu(111) is placed ~0.8Å too high) [36, 37]. This corroborates our interpretation of the formation of MoS_2 islands. XPS of a MoS_2 covered Cu(111) shows a Mo $3d_{5/2}$ binding energy of 229.0 eV, very close to literature and NIST data [38, 39] of 229.25 eV with the small difference likely due to the copper substrate diminishing the Mo charge-deficit in the MoS_2 film. In comparison, a similar amount of Molybdenum on Cu(111) in the absence of sulfur loading was found to have a $3d_{5/2}$ binding energy of 228.2 eV. Fig 2.3 shows a detailed spectrum.

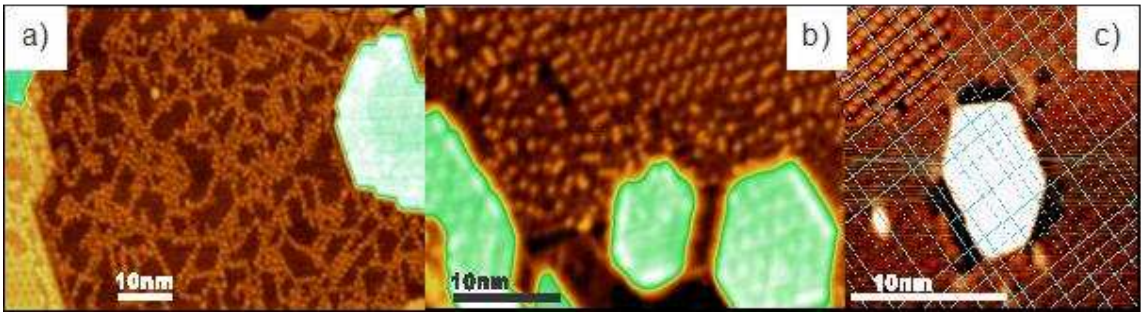

Fig 2.1 Depletion of substrate sulfur loading after sample exposure to Molybdenum and subsequent formation of MoS_2. Depending on the initial sulfur loading and incremental Mo deposition, large terraces are depleted from sulfur (a), disorder is created in the sulfur coverage near MoS_2 islands (b) or individual sulfur atoms are missing (c). Image Parameters: a) Bias: -260 mV, Current: 140 pA; b) Bias: -120 mV, Current: 52 pA; c) Bias: -110 mV, Current: 150 pA.

The size of the MoS_2 islands formed is limited by the amount of Molybdenum deposited and of sulfur loaded on the surface. Depending on the Molybdenum dose, the sulfur depletion extends across large terraces, or is very local. Fig 2.1 shows three examples: a) deposition of Molybdenum reduces the coverage of the prominent sulfur features dramatically over a large sample terrace. Notably, we find that only those sulfur atoms are missing that appear as protrusions in STM. In the literature they are characterized as fourfold sulfur coordination sites; the area between protrusions still contains a very faint structure different from the Cu(111) pattern, presumably due to sulfur atoms differently coordinated by copper. b) Depositing of additional Molybdenum after sulfur loading of a surface that already contains small islands from an initial deposition cycle leads to local depletion of the sulfur loading and converts an ordered sulfur superstructure to a random one. c) If a very small incremental Molybdenum dose is applied, individual sulfur vacancies in the zigzag-row superstructure are revealed.

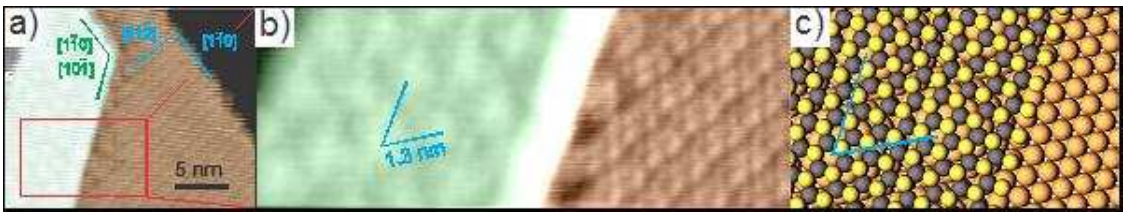

Fig 2.2 (a) portion of a MoS_2 layer (left, green) on a sulfur terminated Cu(111) terrace with a dislocation step indicating substrate crystallographic axes. (b) Enlarged portion near the MoS_2 edge showing angular registry between MoS_2 Moiré pattern and straight edge. (c) atomic model of b highlighting the 1.3 nm Moiré pattern visible in (b). MoS_2 drawn as sulfur terminated; no substrate sulfur superstructure included. Image Parameters: Bias: -560 mV, Current: 140 pA.

The MoS_2 islands and flakes are epitaxial to the substrate in the sense that their crystallographic axes are aligned with the crystallographic axis of the underlayer and that they form a well-defined Moiré pattern. Fig 2.2a shows an extended MoS_2 island running in parallel and at 60° angle to a Cu(111) dislocation line serving as a direct indicator of the substrate high symmetry directions. Fig 2.2b magnifies the vicinity of the MoS_2 step revealing a protrusion at the edge, which was also found for small MoS_2 triangles on Au(111). In that context it was identified as a metallic edge state and discussed with regards to the catalytic properties of MoS_2 triangles. This edge state is observed only at the type of MoS_2 edge depicted (and its two equivalent counterparts at ±120° rotation). Edges at 60° rotation (like at the top of Fig 2.2a) do not feature this edge protrusion. A survey of the edges of many MoS_2 islands shows a preference for the edges that feature this state; In contrast to MoS_2 islands on gold, this preference is not strong enough to render triangular islands dominant: rather a large fraction of the hexagonal islands have sides of unequal length in favor of this edge. Fig 2.2c) follows

Ref. [26] in depicting this edge as terminated with low-coordination sulfur atoms as opposed to high-coordination Molybdenum atoms. The orientation of the MoS_2 layer with regards to the substrate atomic lattice can be deduced from the orientation of the triangles of the Moiré pattern (see Fig 2.2b,c and also Fig 1.4f), as well as from the edges at which the edge state occurs. The latter are oriented in parallel for all MoS_2 islands observed on the single-crystal substrate, indicating that the growth of MoS_2 depends on the location of the second copper substrate layer, which distinguishes between hcp and fcc hollow sites on the fcc (111) face. As a result, the growth of MoS_2 films on Cu(111) is not affected by rotational domains.

To simulate the experimentally observed structure of a MoS_2 layer on Cu(111), we model a supercell consisting of a 5 layer slab of (5x5) Cu(111), a vacuum layer of about 19.5 Å, and a (4x4) layer of MoS_2 adsorbed on one side of the Cu(111) slab. This corresponds to the experimentally observed Moiré pattern. We use the van der Waals density functional (vdW-DF) together with ultra-soft pseudopotential method, which are implemented in the PWSCF package. The Brillouin zone is sampled with (3x3x1) Monkhorst-Pack mesh. The cut-off energy for the plane-wave expansion and for the charge density are respectively 35 Ry and 420 Ry. The structures are relaxed so that all force components acting on each ion are smaller than $4x10^{-4}$ Ry/Bohr. During relaxation of the MoS_2/Cu(111) system, the two bottom layers of Cu(111) slab are kept fixed. The lattice parameters of Cu and of MoS_2 layer are optimized to be 3.690 Å and 3.255 Å, respectively, i.e. the MoS_2 lattice is expanded by <1%, corroborating the experimentally

observed Moiré pattern.

Energy minimization leads to an average distance between the bottom S layer and the Cu(111) surface of ~2.6 Å. We simulate STM image of this sample using the Tersoff-Hamann approximation. In this approach, the total local density of state (LDOS) receives contributions from bands whose eigenvalues lie in the ranges from EF to EF+eV (V>0) or from EF+eV (V<0); where EF, V are respectively the Fermi level and the bias voltage applied to the sample. The isosurface for chosen LDOS provides us the simulated STM image. In this work, we use V=-560mV and isosurface value of 10^{-6} Ry^{-1}. We then calculate the average height of the STM images of MoS_2/Cu(111) and clean Cu(111) surfaces with respect to the position of the topmost Cu layer. The difference between the two heights is the apparent height of the MoS_2 layer. It is ~4.0 Å. Taking into account that the vdW-DF usually overestimates adsorption heights (for example, it predicts the adsorption height of a benzene molecule on Cu(111) to be 0.37 nm when it is expected to be around 0.29 nm), our theoretical prediction is in good agreement with experimental value of 3.22 Å, thus further corroborating our identification of the layer as MoS_2.

Fig 2.3 shows spectra of the Mo 3d region for MoS_2 on Cu(111) prepared as described in the paper as well as for a similar amount of molybdenum on Cu(111) to show the difference. The binding energy is calibrated based on the Cu 2p, 3s and 3p levels. A cubic background has been subtracted. A Gaussian fit is included to guide the eye.

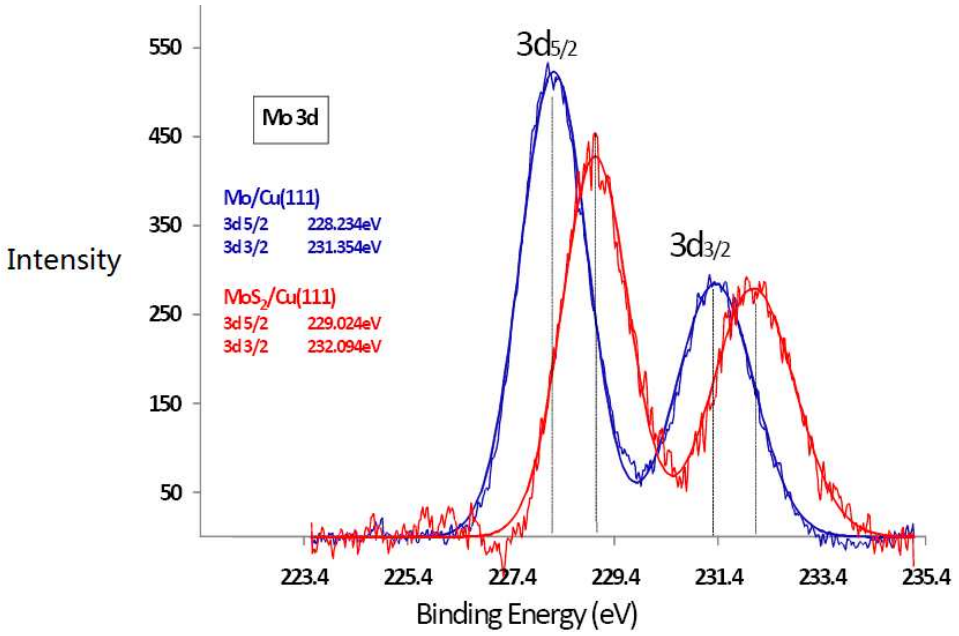

Fig 2.3 x ray photoelectron spectra of MoS_2 on Cu(111) prepared with the same method as the sample prepared in STM.

2.4 Conclusions

In summary, we find that MoS_2 films of tens of nanometers in size can be grown on Cu(111) at moderate temperatures using thiophenol as an easy to handle sulfur source and Molybdenum deposited via e-beam evaporation (physical vapor deposition). Given that electrochemically-prepared copper films are dominantly covered by (111) facets, this process may have potential for application far beyond this single crystal study. Work on extending the islands' size and optimizing the deposition parameters is ongoing.

Chapter 3 Single layer MoS_2 on the Cu(111) surface: First-principles electronic structure calculations

The following is taken from an article I published in Physical Review B: D. Le, D. Sun, **W. Lu**, L. Bartels, and T. Rahman,, Single layer MoS_2 on the Cu(111) surface: First-principles electronic structure calculations, Physical Review B, 2012, 85, 075429. This was collaborative work reporting on measurements by me and other graduate student (D. Sun) Computational support came from D. Le of Talat Rahman's group at the University of Central Florida.

3.1 Introduction

It is well known that a simple material like graphene, which used to be a prototype two-dimensional dream material for theorists, has recently been at the center of fundamental and technical discussions around applications of ultrathin layered materials to nanotechnology.[40] Thanks to its novel properties, it has already found a key application in the high cutoff frequency transistor.[41] Attention has also turned to other layered materials such as transition-metal dichalcogenides,[42] a prototype of which is molybdenum disulfide (MoS_2): a single layer of MoS_2 consists of a molybdenum layer sandwiched between two sulfur layers. The recent finding of the transition of

MoS_2 from an indirect band gap (of 1.2 eV) bulk material or to a direct band gap (~1.8–1.9 eV) in the limit of a single layer [17, 43] makes it a promising new material for industrial applications.[18, 44, 45] This finding has sparked further interest in seeking ways to grow extended layers of MoS_2. Very recently, relatively large single layer patches of MoS_2 were grown on Cu(111),[4] displaying a Moiré pattern, whose periodicity is about 1.3 nm, corresponding to a (5 × 5) Cu(111) surface supercell.

In general, the inhomogeneity in the Moiré pattern suggests a spatial variation of interactions leading to rearrangement of the atoms in the top few layers, as found for graphene [46, 47] and hexagonal boron nitride [48] on metal surfaces. Furthermore, the extent of the buckling is taken to be a quick measure of the interaction of the overlayer atoms with the substrate: small buckling is typically assumed to signify physisorption. What then is the nature of the binding of MoS_2 layer to the Cu(111) surface? To our knowledge this question has yet to be answered. In addition, we would like to examine (1) the size of the Moiré pattern for MoS_2 on Cu(111) and how it compares with that on other close-packed metal surfaces, (2) how the MoS_2 layer stacks on the Cu(111) surface and whether fingerprints from such stacking may be revealed in scanning tunneling microscopy (STM) images, and (3) the extent to which the interaction results in rearrangement of the adlayer or the substrate.

3.2 Experimental Section

3.2.1 Experimental procedures

MoS_2 flakes have been grown in UHV (base pressure <2 × 10^{-10}) by a sequence of deposition of thiophenol onto a sputter-and-anneal cleaned Cu(111) substrate at ~ 100K and 10^{-7} Torr for 300 s, followed by annealing to ~400 K to remove the phenyl groups. Subsequently, Mo metal is deposited using an *e*-beam evaporator (Omicron) with ion suppressor, followed by sample is annealing to ~ 500 K for 20 min, to form MoS_2 flakes in various sizes. Image acquisition proceeded after cool down to 80 K. Further details can be found in Ref. [4]

3.2.2 Computational Details

We performed first-principles electronic structure calculations to evaluate the total energy and electronic structure of the MoS_2 layer on Cu(111) employing the van der Waals density functional (vdW-DF) [49, 50] and the efficient algorithm proposed by Román-Pérez and Soler [51] together with the ultrasoft pseudopotential method, which are implemented in the Quantum ESPRESSO package.[52] In the spirit of the vdWDF method, the exchange-correlation energy of the system contains three terms: the exchange energy E_x^{GGA} from the revised generalized-gradient approximation (GGA) in the form of the Perdew-Burke-Ernzerhof functional (revPBE),[53] the correlation energy E_c^{LDA} calculated using the local density approximation (LDA), and the nonlocal

correlation energy E_c^{nl}. Our model system consists of aMoS_2 layer on a five-layer Cu(111) slab on top of which we have 15 Å of vacuum. We consider three types of surface superstructures: (3 × 3) MoS_2 on (4 × 4) Cu(111), (4 × 4) MoS_2 on (5 × 5) Cu(111), and (5 × 5) MoS_2 on (6 × 6) Cu(111). To obtain the equilibrium configuration for a given structure, we bring the MoS_2 layer close to the Cu(111) surface in small increments; a minimum in energy is found around 2.6 Å. At this height, we initially arrange the MoS_2 layer such that one S atom sits on a high symmetry substrate site. We then allow all atoms in the system, except for those in the bottom two Cu layers, to undergo ionic relaxation to yield the lowest energy configuration. The two types of hollow sites (fcc and hcp) and the top site lead effectively to three possible stackings of the MoS_2 layer on Cu(111), as we shall see. The Brillouin zone is sampled with a (5 × 5 × 1), (3 × 3 × 1), and (1 × 1 × 1) Γ-centered meshes for the (4 × 4), (5 × 5), and (6 × 6) Cu(111) substrate supercells, respectively. We set the cutoff energy for the planewave expansion to 35 Ry and for the augmentation charge to 420 Ry. All structures are relaxed until all force components acting on each atom reach the 0.01 eV/Å threshold. We find the lattice parameters of bulk Cu and of the MoS_2 layer, estimated by the vdW-DF approximation, to be 3.690 and 3.255 Å , respectively, which are about 2–3% higher than experimental values for Cu (3.61 Å) [1] and MoS_2 (3.16 Å).[54] We calculate the average binding energy E_b per MoS_2 unit according to

$$E_b = \frac{1}{n_1^2}[E_{MoS_2/Cu(111)} - E_{Cu(111)} - E_{MoS_2}]$$

where $E_{MoS_2/Cu(111)}$, $E_{Cu(111)}$ and E_{MoS_2} are the total energy of, respectively, the (n_1 × n_1) MoS_2 on the (n_2 × n_2) Cu(111) system, the clean (n_2 × n_2) Cu(111) slab, and the (n_1 × n_1) free-standing MoS_2 film.

3.3 Results and Discussions

3.3.1 Moiré pattern periodicity

As is known, Moiré pattern results from the mismatch between the intrinsic periodicity of the overlayer and the substrate. This mismatch for an (n_1 × n_1) superstructure on (n_2 × n_2) close-packed metal (*M*) substrate unit, may be defined conveniently by a parameter:

$$m = \frac{n_1 d_s}{n_2 d_m} - 1$$

where d_S is the lattice parameter of the overlayer and d_M is $a_M/\sqrt{2}$ for fcc metal, and a_M for hcp metals, where a_M is the metal lattice parameter. From geometric consideration, the smaller the value of this parameter, the smaller would be the stress in the surface. For Cu(111), the experimental lattice parameters yield d_{Cu} at about 2.255 Å and *dS* for MoS_2 is around 3.16 Å . If we limit n_2 to 20, we find the (4 × 4) overlayer on a (5 × 5) substrate supercell to have the lowest absolute value of *m* (−1.0%). This result agrees very well with the size of Moiré unit cell observed in a recent STM experiment.[4] The two nearest-sized supercells to the preferred one, (5 × 5) MoS_2 on (6 × 6) Cu(111) and (3 × 3) MoS_2 on (4 × 4) Cu(111), have *m* of 3.2% and −7.2%, respectively. Interestingly,

several other close-packed metal surfaces offer an even smaller value of m for a MoS_2 layer. A summary of our calculated minimum value of m corresponding to the ($n_1 \times n_1$) MoS_2 structure over the ($n_2 \times n_2$) metal unit cell ($n_2 \leq 20$) is presented in Table 1.

Surfaces	d_M (Å)[a]	n_1	n_2	m (%)
Ag(111)	2.89	10	11	−0.7
Cu(111)	2.55	4	5	−1.0
Ni(111)	2.49	11	14	−0.2
		15	19	0.2
Pt(111)	2.77	7	8	−0.2
Rh(111)	2.69	6	7	0.8
		11	13	−0.5
		17	20	0.0
Ir(111)	2.72	6	7	−0.2
Re(0001)	2.76	7	8	0.2
Ru(0001)	2.71	6	7	−0.1

Table 1 Predicted sizes of MoS_2 Moiré unit cell on several close-packed metal surfaces ($n_2 \leq 20$).
[a]Calculated from experimental lattice parameters.[1]

As further quantification of the Moiré pattern periodicity, we find the calculated average binding energy of the appropriate MoS_2 structure for the (4 × 4), (5 × 5), or (6 × 6) Cu(111) substrate unit cell to be, respectively, −0.03, −0.27, and −0.16 eV. Once again, the average binding energy is lowest for (4 × 4) MoS_2 on (5 × 5) Cu(111), in agreement with experimental findings.[4]

3.3.2 Geometry of MoS_2 on Cu(111)

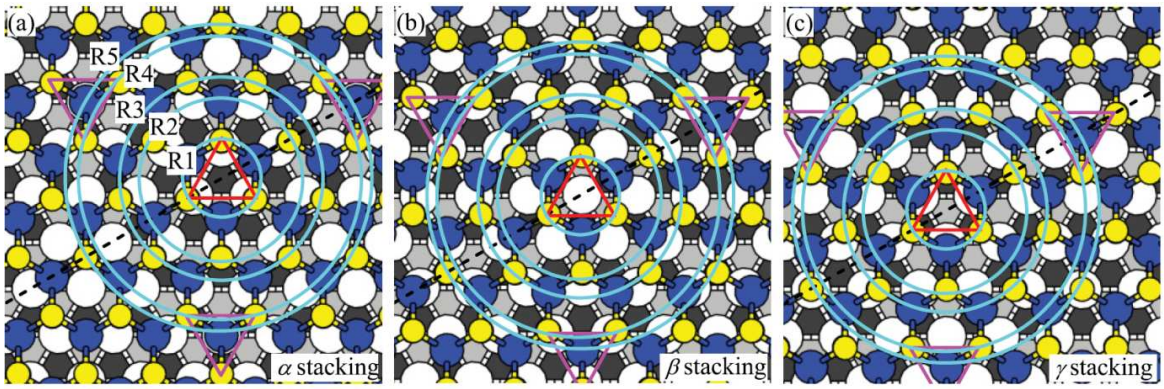

Fig 3.1 Atomic model of a single layer MoS_2 in*α*(a),*β*(b), and*γ*(c) stacking on Cu(111). Yellow (gray), blue (dark), and white circles represent S, Mo, Cu surface atoms, respectively. The dark and light gray spaces between Cu surface atoms are, respectively, fcc and hcp sites of the Cu(111) surface. Rings numbered from R1 to R5 highlight the equivalent S atoms. Triangles highlight groups of three equivalent S atoms. Dashed lines indicate the direction of the shifts between stacking types.

Turning our attention to the most favorable structure, the (4 × 4) MoS_2 on (5 × 5) Cu(111), we first note that after ionic relaxation, three types of stacking (Fig 3.3) are produced. In these, labeled as *α*, *β*, and *γ* , the high-symmetry center is in registry with, respectively, the fcc hollow, top, and hcp hollow site on Cu(111). Here, the high-symmetry center is defined as the center of the smallest up-pointing triangle in Fig 3.1 whose vertices are three equivalent S atoms. The average binding energy of the MoS_2 film on Cu(111) is −0.27 eV irrespective of the stacking type. From the centers of the high-symmetry regions, one can plot five rings, labeled R1 to R5, with radii 1.86, 3.73, 4.95, 6.78, and 7.54 Å (*α* stacking) so that each ring goes through equivalent S atoms. These radii are 1.89, 3.80, 4.99, 6.80, and 7.53 Å for *β* stacking and 1.90, 3.76, 5.00, 6.79, and 7.53 Å for *γ* stacking. The number of interfacial S atoms on each ring is,

respectively, 3, 3, 6, 6, and 3. The S atoms in R5 are in registry with the hcp, fcc, and top sites in the *α*, *β*, and *γ* stacking, respectively. The distance of the S atoms of the lower layer on each ring to their closest Cu atom are, respectively, 2.47, 2.57, 2.70, 2.95, and 3.04 Å in *α* stacking, 2.95, 2.57, 2.70, 2.47, and 3.06 Å in *β* stacking, and 2.82, 2.95, 2.56, 2.81, and 2.46 Å in *γ* stacking. These distances are larger than the typical S-Cu bond-length (2.22–2.29 Å, depending on adsorption sites) [31, 55] for Cu(111).

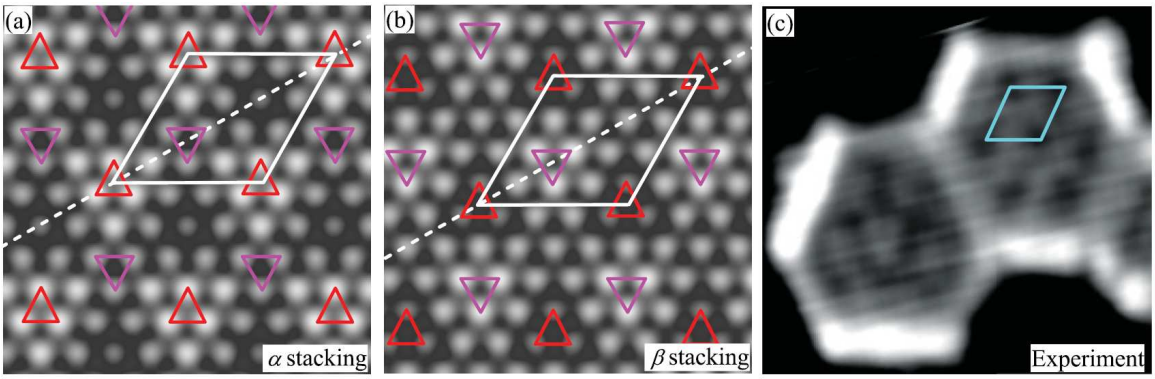

Fig 3.2 (a) and (b) 19 × 19 Å^2 simulated STM image [3]of *α* and *β* stacking. The color scale goes from dark to bright corresponding to the height from 0 to 0.34 Å . Bias voltage is −0.560 V and iso LDOS value is 10^{-6} Ry^{-1}. A 7 × 7 ×1 mesh is used to sample the Brillouin zone. Up- and down-pointing triangles highlight the three spots with the same contrast and corresponding to those in Fig3.1. Parallelograms indicate the Moiré unit cells. (c) STM image of two adjacent MoS_2 islands for comparing the difference in appearance of the Moiré pattern to panels (a) and (b). The parallelogram indicates the Moiré unit cell. The image size is 11.5 nm × 10.5 nm, the bias is −0.475 V, and the tunneling current is 110 pA.

Note that the choice of the center of the high-symmetry region is not unique. In fact, in each Moiré pattern unit cell there is another high-symmetry point (down-pointing triangle in Fig 3.1) in which a Mo atom is centered over a substrate Cu atom (*α*), hcp hollow(*β*), or fcc hollow(*γ*). We opted to choose the center of up-pointing triangles because the footprints of the vertices of these triangles can be distinguished easily in the simulated STM images [Figs. 3.2a and 3.2b]: they are the brightest spots in the *α*

stacking case, the least bright in the *β* stacking case, and neither the least bright nor the brightest in the *γ* stacking. On the other hand, the vertices of down-pointing triangles are displayed as the brightest spots in the *β* case, less (but not the least) in the *α* case, and the least bright in the *γ* case. Regardless, the analysis above provides fingerprints for identifying stacking types from high atomic resolution STM images of MoS_2/Cu(111) systems: for images, recorded at voltage of about −0.5 V, if the brightest spots are the vertices of the smallest up-pointing triangles (with respect to the orientation shown in Fig 3.1), the stacking is *α* type, if they are those of the down-pointing triangle it is *β* type, otherwise it belongs to *γ* type.

The existence of different types of registries of MoS_2 layer with Cu(111) is also seen in experimental STM images of MoS_2 flakes on Cu(111). Fig 3.2c shows two adjacent MoS_2 islands in the same orientation as in Fig 3.1. One threefold degenerate MoS_2 edge appears as protrusions in STM because it contains an extra sulfur atom.[56] Inside the islands, the Moiré pattern is visible and clearly different in appearance as predicted in this study.

3.3.3 Interaction between MoS_2 and Cu(111)

The relatively large separation (∼2.6 Å) of the bottom S layer and the Cu(111) surface (see Fig 3.3) and the low binding energy per MoS_2 unit (−0.27 eV) would at the outset imply a weak interaction, which in turn suggests a small corrugation of the film. Detailed analysis of intralayer buckling—the difference between the *z* coordinate of the

highest and the lowest atoms of the topmost S layer—at ~0.06–0.07 Å is much smaller than that known, for example, for graphene on most substrates.[57] Our calculations also find similar low values for the buckling of the lower S and the Mo layers. Interestingly, the buckling of the top three Cu layers is larger, at 0.29, 0.23, and 0.10 Å, respectively. A similar trend is found for the other two cases, i.e., (3 × 3) MoS_2 on (4 × 4) Cu(111) and (5 × 5) MoS_2 on (6 × 6) Cu(111).

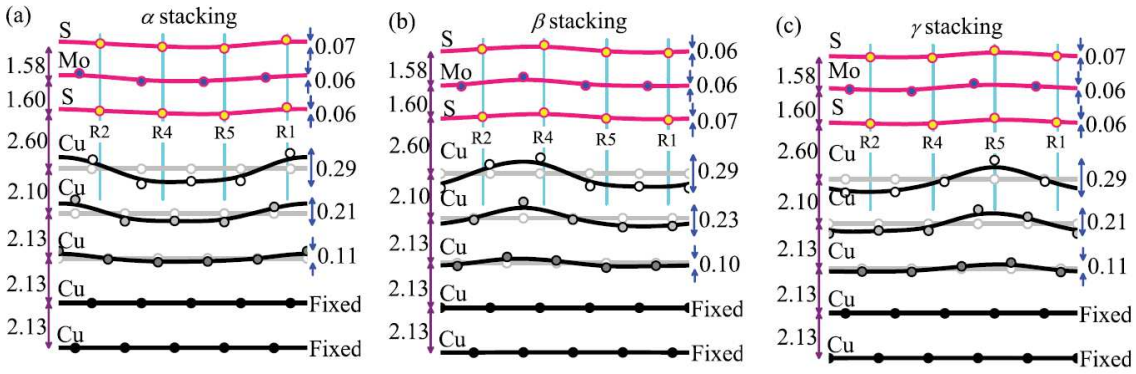

Fig 3.3 Intralayer buckling along the long diagonal of Moiré unit cells of *α*(a), *β*(b), and *γ* (c) stacking. Circles represent S, Mo, and Cu atoms. *B*-spline fits (solid lines) are included for eye guidance purpose. Vertical lines point out relative positions of the rings R1, R2, R4, and R5. The numbers (in Å) in the left and right are the average *interlayer* distances and the buckling of layers.

There appears to be a correlation between the ripple of the Cu layer and the brightness of the spots in the simulated STM images in Fig 1. The periodic ripple of the Cu(111) surface leads to the inhomogeneity in interaction between the Cu surface and MoS_2, which is, in turn, represented by the displacement of Cu atoms on the top layer. The more they move up toward the MoS_2 layer, the stronger is the interaction between MoS_2 and the Cu surface. In Fig 3.3, one can see that themodulation of the Cu surface in the *α* stacking is the largest near ring R1, resulting in the brightest spots in the simulated

STM image. And it is the smallest near rings R5 and R4 causing less bright spots. A similar effect can also be seen for the case of *β* stacking in which the largest modulation of the Cu surface is near ring R4 corresponding to the brightest spots in its STM image and the least modulation is near ring R1 resulting in the least bright spots. In the case of *γ* stacking, the largest modulation of Cu(111) is at ring R5 and the smallest modulation is near ring R2 and R4 leading to the brightest and less bright spots in STM image, respectively.

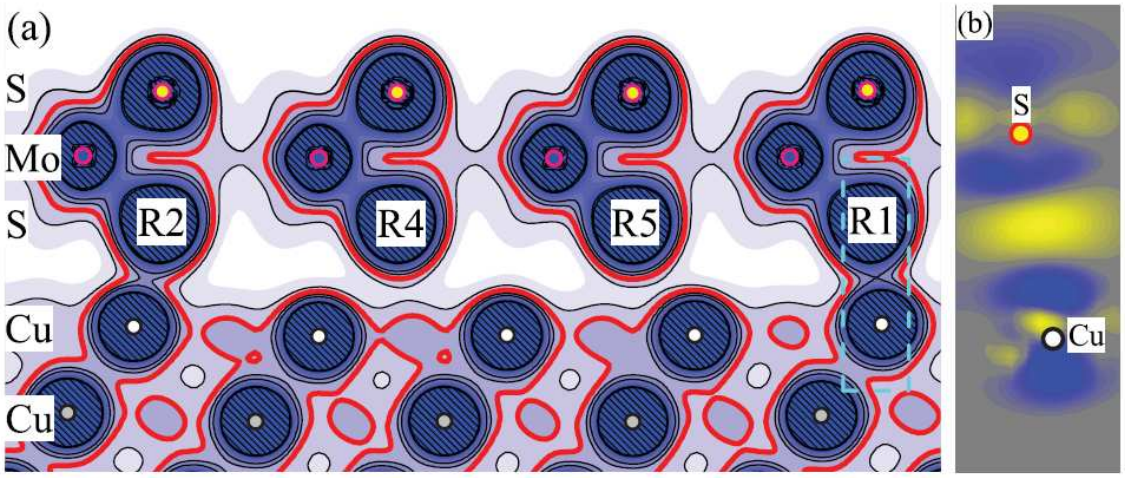

Fig 3.4 (a) Valence charge density along the vertical plane passing through the long diagonal of the Moiré unit cell of the *α* stacking of MoS_2 on Cu(111). R1, R2, R4, and R5 indicate the rings [see Fig 3.1a] to which S atoms belong. The labels (S, Mo, Cu) on the left map the rows of S, Mo, and Cu, respectively. Contour values are 0.02, 0.03, 0.04, 0.05, and 0.09 au. The 0.03 contour is highlighted (the thickest line) for guidance the eyes. (b) Density of redistribution of charge in the region limited by a broken rectangular in panel (a). Yellowish (bright) and blueish (dark) regions indicate, respectively, accumulation and depletion of charge. The gray background corresponds to zero redistribution. The scale going from blue (dark) to yellow (bright) corresponds to the variation from -7.5×10^{-3} to 7.5×10^{-3} a.u.

Another indication of the inhomogeneous interaction between the MoS_2 layer and the surface Cu atoms is seen in the plot of the charge-density distribution, Fig 3.4a (*α* stacking as an example), which shows an appreciable amount of charge in the region

between the S atoms in rings R1 and R2 and their nearest Cu surface atoms but not much in the region near the other rings. Calculated charge redistribution upon adsorption of MoS_2 on Cu(111), Fig 3.4b, confirms a noticeable accumulation of charge in these regions. This is a signal of chemical bonding—albeit weak—between S in ring R1 and Cu atoms. A similar type of bonding is also formed between S in ring R2 and Cu atoms.

3.4 Conclusions

In conclusion, our calculated optimum size of the Moiré pattern is in agreement with experimental observations. We have also predicted the size of Moiré patterns for MoS_2 on several close-packed metal surfaces by minimizing their mismatch parameters. We show the presence of three energetically equivalent stacking types (α, β, andγ) of MoS_2 on Cu(111) with distinguishable fingerprints in their STM images. Our structural analysis displays very little corrugation of the MoS_2 layer but noticeable rearrangement of the Cu surface atoms. More importantly, we find the MoS_2 overlayer to be chemisorbed, albeit weakly, to the Cu(111) surface.

Chapter 4 An MoS_x Structure with High Affinity for Adsorbate Interaction

The following is taken from an article I published in Angewandte Chemie: D. Sun, **W. Lu**, D. Le, Q. Ma, M. Aminpur, M. A. Ortigoza, S. Bobek, J. Mann, J. Wyrick, L. Bartels, and T. Rahman, An MoS_x Structure with High Affinity for Adsorbate Interaction, Angewandte Chemie, 2012, 51(41), pp 10284-10288. This was collaborative work reporting on measurements by me and other graduate student (D. Sun, Q. Ma, S. Bobek, J. Mann, J. Wyrick) Computational support came from D. Le, M. Aminpur and M. A. Ortigoza of Talat Rahman's group at the University of Central Florida.

4.1 Introduction

MoS_2 is an intriguing material: although its basal plane is quite inert, it is the key catalyst for petrochemical hydrodesulfurization (and hydrodenitrogenation) processes. Dow/Union Carbide developed an MoS_2-based catalyst[58] for the formation of higher alcohols from syngas, an application which is gaining increased importance with the emergence of biofuels. In these applications, MoS_2 is used as a fine powder; cobalt or nickel (or mixtures thereof) activate the powder through incorporation into edges of the MoS_2[59-61] structures. Further promotion is achieved by alkali doping with carbon typically serving as the support.[62-64] Quite recently, MoS_2 has attracted increasing interest as an exfoliatable monolayer material for (opto-)electronic applications,[17,

43] and as a surface material for electrochemical reactions,[65] among other applications.

Several studies have succeeded in growing MoS_2 on various substrates and have shown that its catalytic activity may be ascribed to a metallic electronic state at the brim of MoS_2 triangular clusters, which can be readily identified in scanning tunneling microscopy (STM).[56, 66-73] We have recently developed a technique for growing MoS_2—by evaporating molybdenum on a sulfur-preloaded Cu(111) surface—that leads to epitaxial MoS_2 islands of sizes ranging from approximately 1 to 100 nm and for which we have confirmed the presence of the brim state.[4] Herein, we demonstrate that another novel MoS_x structure, reproducibly formed in the same fashion as in the growth of MoS_2 we recently performed, is stable in the entire temperature range of our experiments (25 K to 650 K) and reverts to its pristine form after exposure to oxygen-containing adsorbates upon annealing. More importantly, this structure interacts far more strongly with these adsorbates than MoS_2. Analysis of STM images and related electronic structure calculations confirm the metallic nature of this monolayer material, which we rationalize below to have the composition Mo_2S_3.

We chose anthraquinone (AQ) as test adsorbate, because it is large and rigid enough that we can directly image its adsorption geometry, from which we can derive insight into the interaction of the surface with the adsorbate.

4.2 Experimental Section

Growth of MoS_x structures on Cu(111) under ultra high vacuum conditions involves a sequence of sulfur-enrichment of the surface through exposure to benzenethiol at 100 K and 10^{-7} Torr, followed by deposition of Mo from an e-beam evaporator while maintaining the benzenethiol pressure at 10^{-9} Torr. Finally, the surface is annealed to 650K.

Density-functional-theory (DFT) modeling of the surface structure as well as of AQ adsorption is carried out using the VASP code.[12] We use the pseudo-potential approach, taking into account 11, 6, 6, 6, 4, and 1 outermost electrons for Cu, Mo, S, O, C, and H elements, respectively. We use the Projector-Augmented-Wave (PAW) method [74-76] pseudo-potentials with the opB88 version of the exchange functional and the non-local correlation functional by Dion *et al*.[49] as implemented in VASP by Klimeš *et al*.[77] The functional constructed in this manner (vdW-DF) has been shown to be accurate in the treatment of systems dominantly bonded by dispersion-forces[4] and to provide good agreement [78] with the adiabatic-connection fluctuation-dissipation theorem (AC-FDT) in the random phase approximation (RPA),[79] but has so far not been tested with aromatic system of the complexity investigated here. We use the Román-Pérez and Soler algorithm [51] to speed up the calculation of the non-local correlation energy. We cut off the plane-waves expansion of the Kohn-Sham orbitals at 500 eV and the kinetic energy for augmentation of charges at 2000 eV. The Brillouin

Zone is sampled by uniform meshes with grid spacing of ~0.02 to 0.05 $Å^{-1}$, depending on the sizes of simulation supercells. We converge the total energy of any ionic configuration to 0.1 meV, and optimize the systems by minimizing the forces on the atoms to 0.03 eV/Å. In all calculations we model the Cu(111) substrate with a 5-layer-thick slab separated from its periodic images by ~ 20 Å.

4.3 Results and Discussions

The sample preparation gives two thermally stable MoS_x patterns (Fig 4.1a). The patches formed by both patterns are capable of extending across substrate steps. Regions not covered with an MoS_x patch exhibit the well-known (√7 × √7) R19° Cu–S overlayer (abbreviated √7 in the following) that forms on Cu(111). Although this Cu–S overlayer has been studied extensively both experimentally and through calculations, its atomic-level setup remains in debate.[29, 30, 80-85] Our DFT calculations of the vibrational spectra at the surface Brillouin zone center (*Γ*) for some of the proposed hexagonal √7 sulfur terminations of Cu(111) show both the structure reported by Domange and Oudar[80] and the Cu_4-based structure studied by Foss[29] to be dynamically stable. Although the phonon densities of states at *Γ* show structure-distinctive frequencies, the differences between the two spectra are too subtle to determine an energetic difference. In the following, we assume that the structure proposed by Domange and Oudar is correct (Fig 4.1c), because experimental and theoretical work supports it so far.

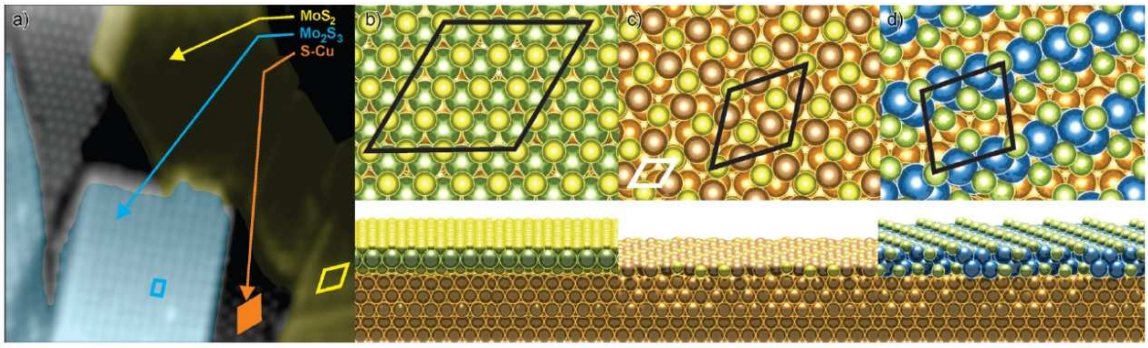

Fig 4.1 STM image of MoS*x* structures. Models of b) MoS_2/Cu(111), c) √7 sulfur-terminated copper (S–Cu), and d) Mo_2S_3 structure at the focus of this manuscript. Imaging parameters: bias: −0.93 V, current: 0.21 nA, scale bar: 5 nm. Models: Cu=brown, S=yellow, Mo=green/blue.

MoS_2 is one of the MoS_x patterns we observed (Fig 4.1b). All MoS_2 films and islands were found to align with the crystallographic axes of the substrate, and they appear in STM with a characteristic Moiré pattern caused by the epitaxial growth of (4×4) unit cells of MoS_2 on (5×5) atoms of the Cu(111) substrate (Fig 4.1b).[4] These islands also feature the electronic brim state, described in detail by Besenbacher and co-workers for MoS_2 synthesis on gold,[56, 86] to which the catalytic activity of MoS_2 has been attributed.

The other MoS_x pattern corresponds to well-ordered islands that have a unit cell with √7-long sides (similar to the hexagonal √7 structure), but at angles of 82° and 98°—or $\begin{bmatrix} 2 & 1 \\ -2 & 3 \end{bmatrix}$ in vector notation. The pattern provides the closest approximation to a square unit cell achievable with short unit vectors on an fcc(111) surface. Although a number of molybdenum–sulfur structures have been described (including bulk Mo_2S_3),[69, 87-89] to our knowledge, there is no prior reference to this nearly square

structure. We found up to 20□% of the sample surface covered by this structure. After a thorough computational screening of about 50 possible MoS_x structures on Cu(111), targeted to find the lowest-energy structure and the one whose calculated STM image most resembled the observed one, we found good correspondence of these nearly square patches with the properties of an Mo_2S_3 layer (Fig 4.1□d). In the following, we will describe some observations (experimental and computational) that support this structural model and will highlight its chemical properties. The geometry that we found to best match our experimental observations while at the same time being structurally stable on Cu(111) contains four molybdenum atoms and six sulfur atoms $\begin{bmatrix} 2 & 1 \\ -2 & 3 \end{bmatrix}$per unit cell (i.e., Mo_2S_3); it arranges the molybdenum atoms in approximately an upright square which is stabilized along its sides by the sulfur atoms (Fig 4.1□d).

As we were not aware of any precedence for this MoS_x structure, establishing its unit cell composition and internal geometry was not trivial: diffraction was no help here, as both the √7 sulfur termination of copper and the novel structure are set up from √7 unit vectors and coexist on the surface. We validated the presence of molybdenum in this structure in preparations identical to the one mentioned in preparation procedure, yet leaving out the deposition of molybdenum resulted in the formation of exclusively the √7 sulfur termination of copper. We note that surrounding the MoS_2 islands we frequently found sulfur depletion of the √7 structure.[4] This is, however, not the case around the Mo_2S_3 islands, in agreement with their lower sulfur surface density (Fig 4.1□d).

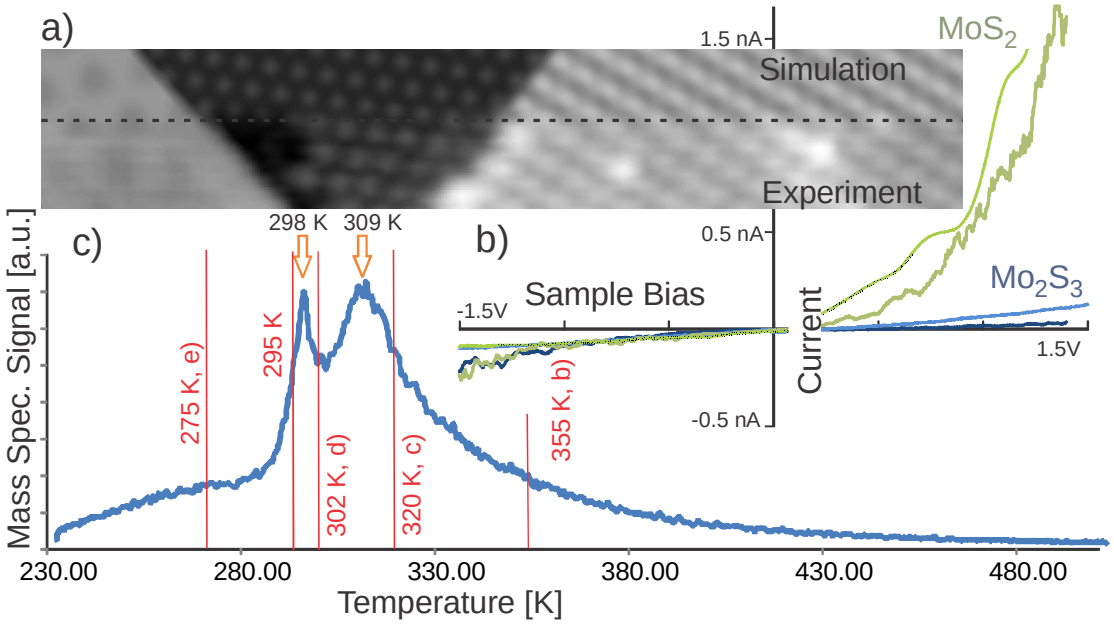

Fig 4.2 STM image (below the dashed line) and simulation (above the dashed line) of a sample with MoS_2, S–Cu, and Mo_2S_3 (left to right) in a single scan line. Also shown is depletion of the S–Cu surface directly adjacent to the MoS_2 island (white arrow). Scale bar: 1 nm; tip height stabilized at 0.15 nA at −1.04 V bias. b) I/V spectra obtained on MoS_2 and Mo_2S_3 (darker lines), and simulated I/V curves (lighter lines); same imaging conditions as above. c) Thermal desorption spectroscopy of AQ fragments (masses: 50, 77) shows two signals corresponding to AQ adsorbed on $MoS_2$and √7 S–Cu, and a high-temperature shoulder for desorption from the two configurations on Mo_2S_3. The red labels indicate the STM images that can be obtained after annealing to these temperatures by referring to the panels of Fig 4.4.

Fig 4.2a shows an STM image in which all three structures are present adjacent to each other in a single scan line: on the left is an MoS_2 island, in the center the √7 sulfur-terminated copper, and on the right an Mo_2S_3 patch. Also visible is some depletion of the √7 × √7 R19° sulfur atoms directly adjacent to the MoS_2 layer. The top portion of that image is DFT-derived simulated topography as an isosurface of energy-integrated (from −1.0 to 0 eV) local density of states of 10^{-4} e/Å^3 convoluted with a tip radius of 2.4 Å. While each structure was calculated separately (hence not showing any edge effects), the relative heights of the structures were referenced to the

bottommost of the five substrate layers in the DFT simulation, thus permitting no adjustable parameter in the height profile between simulation and experiments (both image portions use the same grayscale). Not only are the relative heights reproduced well, but even subtleties, such as the amplitude and alignment of the Moiré pattern on the MoS_2, are represented convincingly.

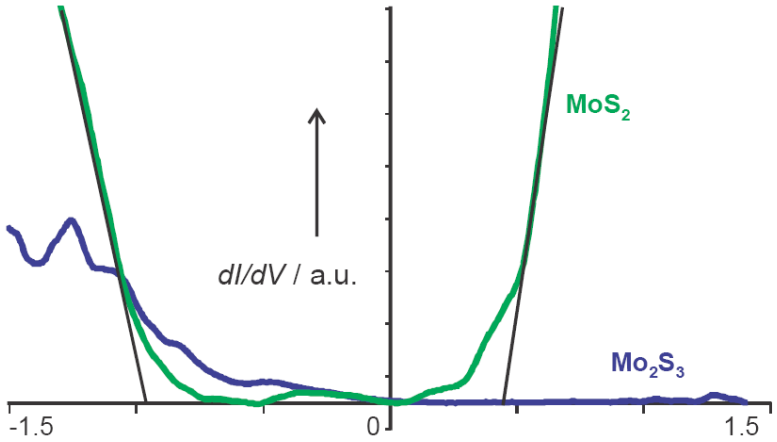

Fig 4.3 dI/dV spectra acquired using a modulation voltage of 20 mV at 800 Hz and an initial setpoint for the tip height at -1.04V sample bias and 0.15 nA. MoS_2 exhibits a bandgap of ~1.4 eV, whereas no bandgap can be made out for Mo_2S_3.

Scanning tunneling spectroscopy performed on MoS_2 and Mo_2S_3 layers resulted in fundamentally different spectra (Fig 4.2b): on MoS_2 we found comparatively little variation of the tunneling current at negative sample bias, but large variation at positive bias, indicating the MoS_2 conduction band edge. In contrast, on Mo_2S_3 we found little variation of the current at either polarity, attesting to the absence of band edges near the Fermi level, in agreement with DFT simulations, which were averaged over the Mo_2S_3 unit cell area. Fig 4.3 contain d*I*/d*V* spectra, which indicate a bandgap of approximately 1.4 eV for MoS_2, in good agreement with recent studies on MoS_2 devices

with metallic contacts.[18, 90] The comparatively high abundance of the Mo_2S_3 layer posed the question of its relevance for surface reactions and surface catalytic activity. To elucidate the capability of this structure to interact with adsorbates, we exposed it to a molecular species, anthraquinone (Fig 4.4), which was chosen for ease of imaging in STM.

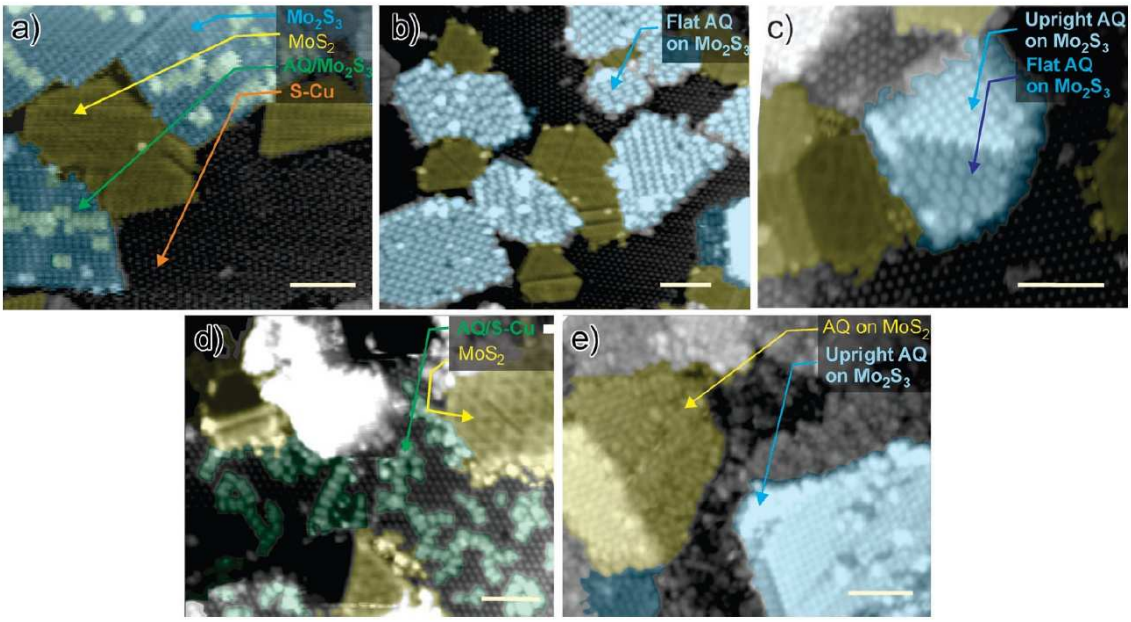

Fig 4.4 STM images of increasing AQ coverages on the different surface structures (panels b–e correspond to 0.1, 0.3, 1.5, and 2.7 Langmuir, respectively). Initially, AQ forms a) rows on Mo_2S_3, followed by a complete coverage of Mo_2S_3 with first b) horizontally and next c) uprightly adsorbed molecules. Only subsequently do d) molecular rows form on the √7 structure until finally e) MoS_2 is covered. The scale bars are 5 nm. Imaging parameters: a) bias: −4.33 V, 0.24 nA b) bias: −1.66 V, 0.17 nA; c) bias: −0.83 V, current 0.34 nA; d) bias: −0.92 V, current 0.11 nA; e) bias −2.75 V, current: 0.13 nA.

Fig 4.4 shows images obtained on the same surface at increasing exposure of AQ from panels b to e. Exposure proceeded at near-liquid-nitrogen temperature followed by annealing just below room temperature. Contrary to our expectation of preferential adsorption of AQ at the brim states of MoS_2, we found AQ to adsorb exclusively at the

Mo_2S_3 structure (Fig 4.4a). Initially, AQ forms molecular rows at intermolecular distances of √7, quite similar to AQ rows on Cu(111) (and on the √7 structure, see below), for which we found the presence of non-negligible intermolecular hydrogen bonds.[91-93] On further increasing the dosage of AQ, we observed an increase in the coverage exclusively on the Mo_2S_3 structure until a dense layer of AQ molecules, adsorbed parallel to the substrate (Fig 4.4b), is formed. Increasing the coverage further leads to a denser packing of the AQ layer on the Mo_2S_3 structure (Fig 4.4c), and the AQ molecules continue to avoid the sulfur-terminated substrate, as well as the MoS_2 islands, with their supposedly reactive brim states.

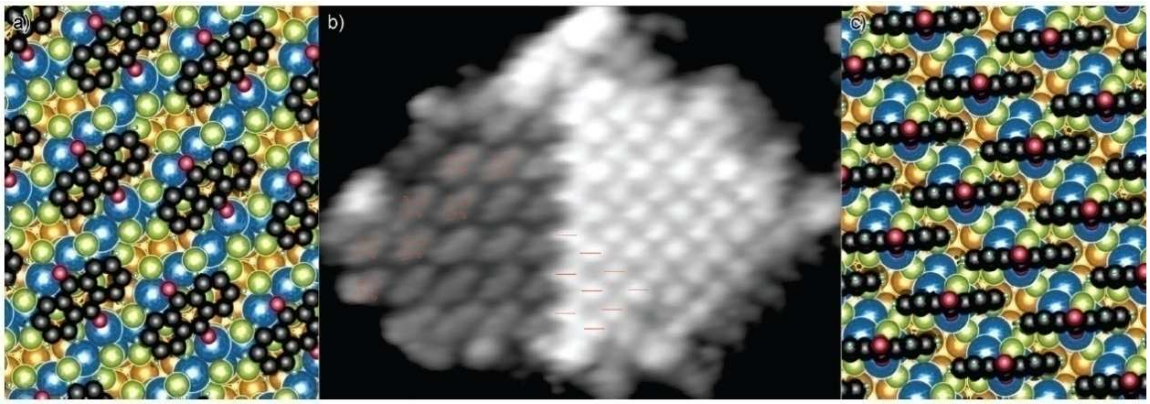

Fig 4.5 a, c) DFT-optimized adsorption geometry of AQ on Mo_2S_3 in horizontal and vertical adsorption configuration, respectively, and b) STM image (magnification of the island in Fig 3c) showing the coexistence and relative orientation of the molecules. Imaging parameters: bias=−0.83 V, current=0.34 nA, scale bar: 5 nm.

We performed DFT simulations of the two adsorption configurations of AQ on Mo_2S_3 that we observed experimentally: in agreement with the experimental observations, minimization of the adsorption configuration results in registry, periodicity, and alignment (Fig 4.5). In the planar configuration, both AQ carbonyl groups are in close proximity to the top molybdenum atoms of the Mo_2S_3 structure (Fig 4.5a); in the

upright configuration, the bottom carbonyl group adsorbs on one of the molybdenum centers, resulting in a slight rearrangement of the Mo_2S_3 structure (Fig 4.5c). We find the binding energy to be 3.36 eV and 1.92 eV in the planar and upright configuration, respectively.

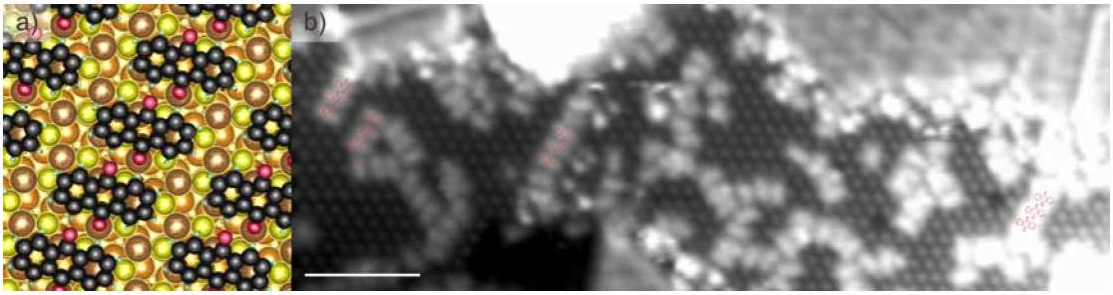

Fig 4.6 a) DFT-optimized adsorption geometry of AQ on the √7 Prince structure. b) STM image of an area covered by the √7 structure between MoS_2 islands showing flat adsorption of AQ. Imaging Parameters: Bias: -919 mV, Current: 220 pA; Scale bar: 5 nm.

Once all Mo_2S_3 is covered, AQ populates the sulfur-terminated copper surface (Fig 3d), including the areas near the MoS_2 and Mo_2S_3 island edges. Here, AQ preferentially forms close molecular rows, optimizing intermolecular hydrogen bonding, as discussed in previous publications.[91-93] Because of the geometry and size of the √7 S–Cu structure and its incommensurability with AQ, molecular rows in adjacent surface unit cells do not generate a closely packed AQ layer (in contrast to what occurs on Mo_2S_3), and we observed the absence of long-range 2D order on this surface. Fig 4.6 contain the calculated adsorption structure and a higher-magnified STM image. The calculated adsorption energy of AQ on the sulfur-terminated copper surface is 1.47 eV, lower than that on the Mo_2S_3 structure, even in the upright configuration.

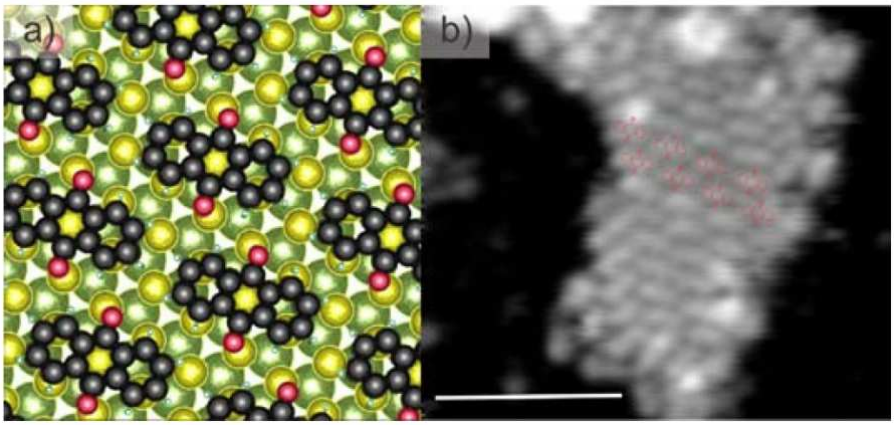

Fig 4.7 a) DFT-optimized adsorption geometry of AQ on MoS_2. b) STM image of a MoS_2 island covered by AQ showing flat adsorption of AQ. Imaging Parameters: Bias: -2753mV, Current: 270 pA ; Scale bar: 5 nm.

AQ molecules only populate the MoS_2 islands and their brim areas after the sulfur-terminated copper surface is covered. Here, AQ preferentially forms an array of molecular rows, which are in anti-phase with adjacent rows, though occasionally in-phase lateral stacking of rows is also observed. The spacing of AQ molecules (at 6.75 Å center to center) is very tight, thus enabling intermolecular hydrogen bonding, as discussed previously.[91-93]

The electronic and optical properties of MoS_2 in the presence of a substrate have already been analyzed by ab initio calculations.[94-97] Because the periodicity of the AQ layer on MoS_2 is incommensurate with the Moiré superstructure of the (4×4) MoS_2 layer, we calculated the adsorption energy of 1.32 eV by modeling an isolated molecule on a MoS_2/Cu slab (1.20 eV) and adding to that the lateral AQ–AQ interactions calculated on a MoS_2 monolayer (0.12 eV). The hierarchy of the DFT adsorption energies is thus in agreement with the relative preference for AQ adsorption on the three different surface structures that we report here. Fig 4.7 contains the calculated adsorption structure.

Thermal desorption spectroscopy of AQ gives the trace shown in Fig 4.2c. Through a sequence of partial annealing and STM imaging, we correlated its features to the structures shown in the referenced panels of Fig 4.4: heating to 275 K results in a complete coverage of the surface (Fig 4.4e); the signal at 297 K corresponds to AQ adsorbed on MoS_2/Cu(111), imaging after heating to 302 K shows AQ only on the sulfur-terminated copper and on Mo_2S_3 (Fig 4.4d); the signal at 309 K corresponds to AQ/S–Cu, and its broad high-temperature tail to the two AQ configurations on Mo_2S_3; imaging at 320 K and 355 K shows AQ exclusively upright and flat (Fig 4.4c and 4.4b), respectively. The absence of a sharp signal and the proximity of the signals of the latter configurations show how these structures may have been overlooked in previous spectroscopic studies. Increase of the substrate temperature above 500 K results in a clean surface with the three surface morphologies shown in Fig 4.1 and 4.2. The sequence of desorption temperatures are in agreement with our theoretical modeling of binding energies; the calculated energy values for all structures are higher than what one would expect from the desorption experiment, thus attesting to the challenges of modeling van der Waals interaction in unit cells of this size and complexity.

The finding of a thermally stable molybdenum–sulfur structure that has higher affinity for adsorbate interaction than the much discussed MoS_2 brims is exciting and suggestive of its relevance to existing catalytic applications, or its utility as an inverse catalyst,[98] yet reactor studies will be necessary to confirm its relevance conclusively. We also attempted to adsorb CO on the MoS_x structures, but could not resolve its image

on the surface, probably because it was moving too rapidly at a sample temperature of approximately 25 K (CO starts diffusing on Cu(111) at around 40 K and the passivated surfaces investigated here offer CO interactions that are weaker than those of metallic copper, as shown in our calculations).[99, 100]

4.4 Conclusions

In conclusion, we found a novel MoS_x surface structure on copper, which we propose to have the composition Mo_2S_3, whose ability to interact and activate adsorbates far exceeds that of MoS_2 while proving to be of similar thermal stability and also recoverable after adsorption through annealing. Some catalyst compositions of MoS_x for the formation of products from syngas contain copper; thus, our finding of a high affinity MoS_x composition specifically on copper may point toward an alternative origin of the actual working of such a catalyst, if further corroborated by studies at high pressure.

Chapter 5 Growth of Aligned Mo_6S_6 nanowires on Cu(111)

The following is taken from an article I published in Surface Science: D. Le, D. Sun, **W. Lu**, M. Aminpur, C. Wang, Q. Ma, L. Bartels, and T. Rahman, Growth of Aligned Mo_6S_6 nanowires on Cu(111), 2013, 611, pp 1-4. This was collaborative work reporting on measurements by me and other graduate student (D. Sun, C. Wang, Q. Ma,) Computational support came from D. Le, and M. Aminpur of Talat Rahman's group at the University of Central Florida.

5.1 Introduction

Molybdenum-sulfide compounds have recently attracted considerable attention for a broad range of applications beyond MoS_2's established function as a lubricant and as a hydrodesulfurization catalyst. Mechanical exfoliation allows access to single layer and few layer MoS_2 films which have properties that are complementary to graphene [21, 101] including a native band gap [17, 43, 96, 102] and valleytronic properties [103-107]. Beyond its catalytic use in controlling the sulfur contents of petrochemical products, its ability to catalyze the formation of alcohols from syngas is also being investigated for production of fuels from biomass. In this context we recently explored the binding of oxygenate species on a new Mo_2S_3 monolayer phase [108]. Work on hybrid compounds

such as $MoO_3/MoS_2$with a core–shell structure shows promise for electrocatalytic application in hydrogen evolution [109-112].

As is the case with carbon, compounds of molybdenum and sulfur may assume a number of nanoscale forms such as nanotubes [113], nanorods [114] and nanoparticles [115, 116]. Here we describe the formation of one-dimensional (1D) Mo_6S_6 features, similar to nanowires reported earlier by Kibsgaard et al. [69] with the difference that our structures are not bundled but well separated from each other. These Mo_6S_6 nanowires display 60°-rotated AB stacking of Mo_3S_3 building blocks consisting of a triangle of Mo atoms decorated with three sulfur atoms at the perimeter (Fig 5.1a,b).

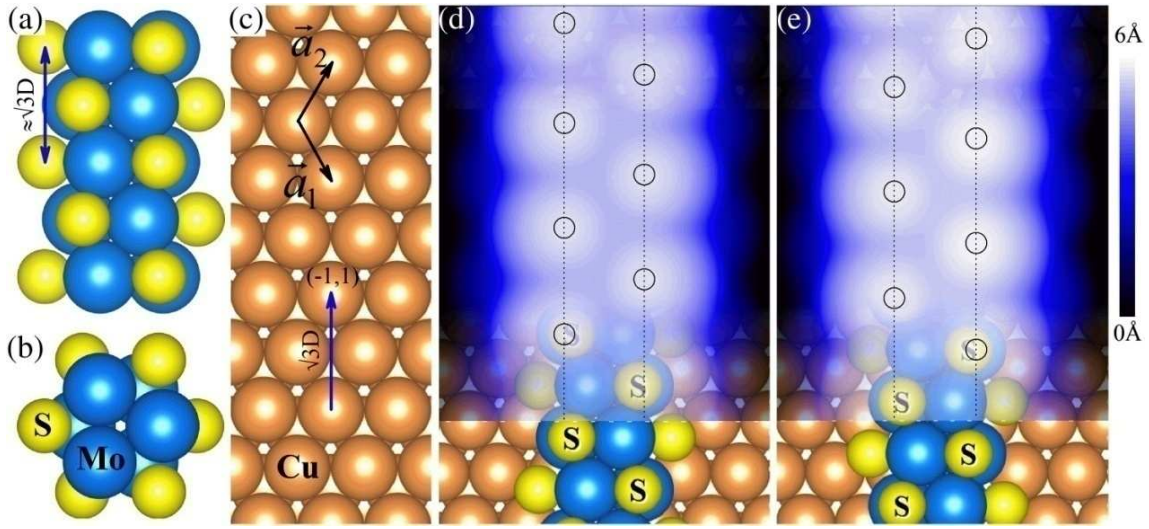

Fig 5.1 Atomic model of Mo_6S_6 nanowires (a, b) and the Cu(111) surface (c). Panels (d) and (e) show models of two potential configurations of Mo_6S_6 nanowires on Cu(111), a symmetric one (d) and an asymmetric one (e). We superimpose simulated STM images, in which we mark the maxima with black circles. While in (d) both maxima have the same height, in (e) the ones on the right are more prominent than those on the left.

Kibsgaard and coworkers [69] grew molybdenum–sulfur nanowire bundles on highly ordered pyrolytic graphite (HOPG); they suggest that their bundles consist of several Mo_6S_6 units side by side. The wires were found to grow in a disordered fashion: substrate interactions appear to be insufficiently strong to align them with the HOPG crystallographic directions. Here we show, theoretically and experimentally, that the use of a more interactive substrate, Cu(111), permits the growth of molybdenum sulfide nanowires that consist of a single stack of Mo_6S_6 units only and that are aligned with the substrate directions. Moreover, we find the preferred spacing between adjacent Mo_6S_6 wires to be slightly larger than their van-der-Waals (vdW) separation distance in the gas phase, highlighting the importance of substrate interactions and suggesting the latter's ability to both align and space the wires evenly. Following Ref. [69], we refer to the features as nanowires even though they are found in the presence of an interactive substrate.

5.2 Experimental Section

All experiments proceeded in a UHV chamber housing a variable temperature scanning tunneling microscopy (STM) setup. The nanowires were grown on a Cu(111) surface initially cleaned by typical sputtering and annealing cycles followed by exposure of the surface to benzenethiol in order to sulfurize it [108]. On the resultant $(\sqrt{7} \times \sqrt{7})R19°$S:Cu surface we deposit a sub-monolayer of Mo using an e-beam evaporator while applying 10^{-9} Torr background pressure of benzenethiol. Subsequent

annealing of the sample to ~ 600 K for ~ 20 min leads to the surface morphologies shown here.

Density functional theory (DFT) simulations are carried out using the projector-augmented wave (PAW) method [117] and a plane-wave basis set which are both implemented in the Vienna Ab Initio Simulation Package [118]. In order to take into account vdW interactions, which are expected to play an important role in the attraction between Mo_6S_6 nanowires, we use the optB88-vdW version [77] of the van der Waals density functional (vdW-DF) [49, 50] to describe the exchange–correlation interaction of the electrons, as implemented in the code of Ref. [119]. The Román-Pérez and Soler algorithm [51] is used for speeding up the evaluation of the non-local energy. The pseudo-potentials are generated using the Perdew–Burke–Ernzerhof (PBE) functional [120] for which 11, 6, and 6 valence electrons are treated explicitly for Cu, Mo, and S, respectively. Tests show that extending the pseudo-potentials to include semicore electrons does not affect the results significantly. We set the cutoff energy for the plane-wave expansion at 500 eV.

For simulating Mo_6S_6 on Cu(111), we use supercells consisting of a 5-layer Cu(111) slab in a $\begin{pmatrix} n & n \\ -1 & 1 \end{pmatrix}$geometry based on the vectors $\vec{a}_1$ and $\vec{a}_2$, as shown in Fig 1c: the 1st and 2nd translational vectors are $n\vec{a}_1 + n\vec{a}_2$ and $-\vec{a}_1 + \vec{a}_2$, respectively. Depending on the nanowire property in question, we employ a supercell that contains either one or two adjacent Mo_6S_6 wires and a vacuum of 20 Å. The Brillouin zone is sampled with a $k \times 13 \times 1$ mesh, where k is 7, 5, and 1 for n equal to 3, 4, and greater than 6,

respectively. During structural relaxations the bottom two Cu layers are held fixed and the calculation terminates when all force-components acting on each free ion are smaller than 0.01 eV/Å. The binding energy of a Mo_6S_6 unit on Cu(111) is calculated as the difference between the total energy of the Mo_6S_6/Cu(111) system and the sum of the total energies of a Cu(111) slab and of a Mo_6S_6 wire which is separated from its periodical images by a distance of 15 Å. We use absolute values of binding energies throughout this manuscript. We simulate scanning tunneling microscopy (STM) topologies as the 10^{-5} e/Å^3 iso-surface of local density of states integrated from −1.0 eV to the Fermi level.

5.3 Results and discussions

Fig 1a and b shows the top and cross-sectional views of the minimal molybdenum–sulfur nanowire that we found to be stable: it consists of Mo-trimers stacked on top of each other at 60°rotation. Each trimer is decorated on the outside with 3 sulfur atoms for a total stoichiometry of Mo_6S_6 (for a pair of Mo_3S_3 subunits at the 60°angle). Fig 1c shows a Cu(111) surface with its basis vectors ($\vec{a}_1$ and $\vec{a}_2$) indicated. Our DFT calculations result in an optimal Cu interatomic spacing of (denoted as D) of 2.564 Å, in excellent agreement with the experimental lattice parameter of bulk Cu [85]. The vertical direction in Fig 1c has a periodicity of √3D, very close to the axial periodicity of Mo_6S_6 nanowires (at a calculated mismatch of ~ 2%), suggesting that Mo_6S_6 nanowires may grow epitaxially along this direction on Cu(111).

We modeled Mo_6S_6 nanowires on a $\begin{pmatrix} 6 & 6 \\ -1 & 1 \end{pmatrix}$ Cu(111) super cell. The distance between the wires and their periodic images is 6D, which is sufficiently large to suppress direct lateral interactions between them (vide infra). The results of structural relaxations indicate two potentially viable configurations: (Fig 5.1d) a symmetric one in which the "S legs" adsorb close to bridge sites and (Fig 1e) an asymmetric one in which half of the "S legs" adsorb close to hollow sites, while the other half adsorb close to bridge sites. The binding energies per Mo_6S_6 unit in the two configurations are 2.61 and 2.59 eV, respectively, slightly favoring the symmetric configuration.

We simulated the STM images expected from these two configurations as the 10^{-5} e/Å^3 iso-surface of local density of states integrated from − 1.0 eV to the Fermi level: in each case, we find a double row of apparent protrusions in anti-phase; the protrusions are centered adjacent to the topmost S atoms (Fig 5.1d,e). In the symmetric configuration, the registries of the topmost S atoms are close to the bridge sites of the Cu(111) surface and the apparent protrusions are very close to the hollow sites (Fig 5.1d). In the asymmetric configuration, half of the topmost S atoms are nearly in registry with the substrate bridge sites whereas the other half are closer to hollow sites and the apparent protrusions are close to bridge sites. Because of the difference in adsorption sites of the two "S legs" in the asymmetric configuration, we predict a small difference of the heights of the topmost S atoms (~ 0.1 Å difference) and, hence, of the protrusions in the STM image.

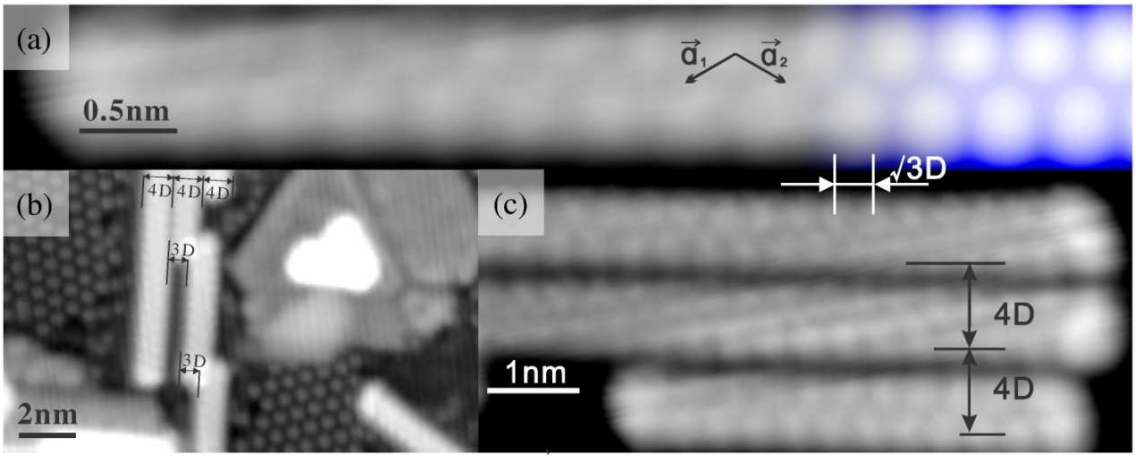

Fig 5.2 STM images (current: 0.13 nA, bias: − 0.82 V) of (a) isolated Mo_6S_6 nanowire on Cu(111) that we blended in the simulated STM image of Fig 5.1d affirming the match between simulation and measurement; (b) overview of our sample preparation showing the nanorods, the sulfur termination of Cu(111) as a hexagonal pattern of apparent protrusions, and MoS_2 islands with characteristic brim state (gray, smooth areas); (c) cluster of aligned and equally spaced Mo_6S_6 nanorods at the 4D separation distance. Vibrations during imaging give rise to the slanted lines in the image.

Fig 5.2 shows our experimental results. The nanowires were grown on a (√7 × √7)R19° sulfur-terminated Cu(111) surface which at the same time also produced MoS_2 and Mo_2S_3 patches [108]. The nanowires are aligned each with one of the three substrate atomic row directions. The nanowires show two rows of protrusion in antiphase along their body, as predicted from our calculations, and additional protrusions at their ends. Within the limits of our experimental observation, no difference in height between the protrusions on one or the other side of the nanowire can be made out, suggesting symmetric adsorption configuration.

Since our growth procedure leaves the Cu(111) surface covered by either sulfur or molybdenum sulfide (MoS_2, Mo_2S_3, or Mo_6S_6), registry information of the nanowires with regards to the bare substrate cannot be obtained. Moreover, the nature of the (√7 × √7)R19° sulfur termination is still under discussion [85]. Assuming the structure

proposed by Foss et al. [29] or by Domange and Oudar [80], the apparent protrusions of the sulfur termination are in registry with the top sites of the underlying substrate. Under this assumption, the protrusions in the STM image are in registry either with the hollow or bridge sites of the substrate supporting both models (symmetry and asymmetry configurations) suggested by our DFT simulations. Given the very small separation distance between hollow and bridge sites, STM images were not able to distinguish them.

In our experiment, we found that the nanowires are grown individually (Fig 5.2a) or in the form of a collinear array at regular spacing (Fig 5.2c). We do not find wires of any other atomic-scale setup or wider cross section. The presence of homogeneous populations (with regards to their cross section) of nanowires with a propensity for regular spacing is exciting. The latter gives rise to the question: what determines the separation distance between adjacent rows? In the absence of a substrate, the separation distance between Mo_6S_6 nanowires is determined by inter-wire interactions consisting mainly of vdW interactions. Using theoretical modeling, the optimal distance can be determined straightforwardly by considering supercells that place adjacent nanowires at different separation distances. We thus performed DFT modeling of nanowires in vacuum and varied the spacing between them. Fig 5.3 shows the resulting interaction potential per Mo_6S_6 repeat unit. For arrangement of adjacent wires both in-phase and anti-phase we find the presence of an optimal separation distance, i.e. a minimum in the interaction potential. The interaction energy at 0.27 eV per Mo_6S_6 unit

is higher for the in-phase than for the anti-phase arrangement (0.18 eV per Mo_6S_6 unit), and the optimal distances are shorter (3.3D as compared to 3.5D, respectively). Notably, we find that when the wires get as close as 3D, their interaction starts to become very repulsive. This suggests that the wires found on HOPG in the work of Kibsgaard and coworkers [69] need to form inter-wire bonds to achieve their close packing.

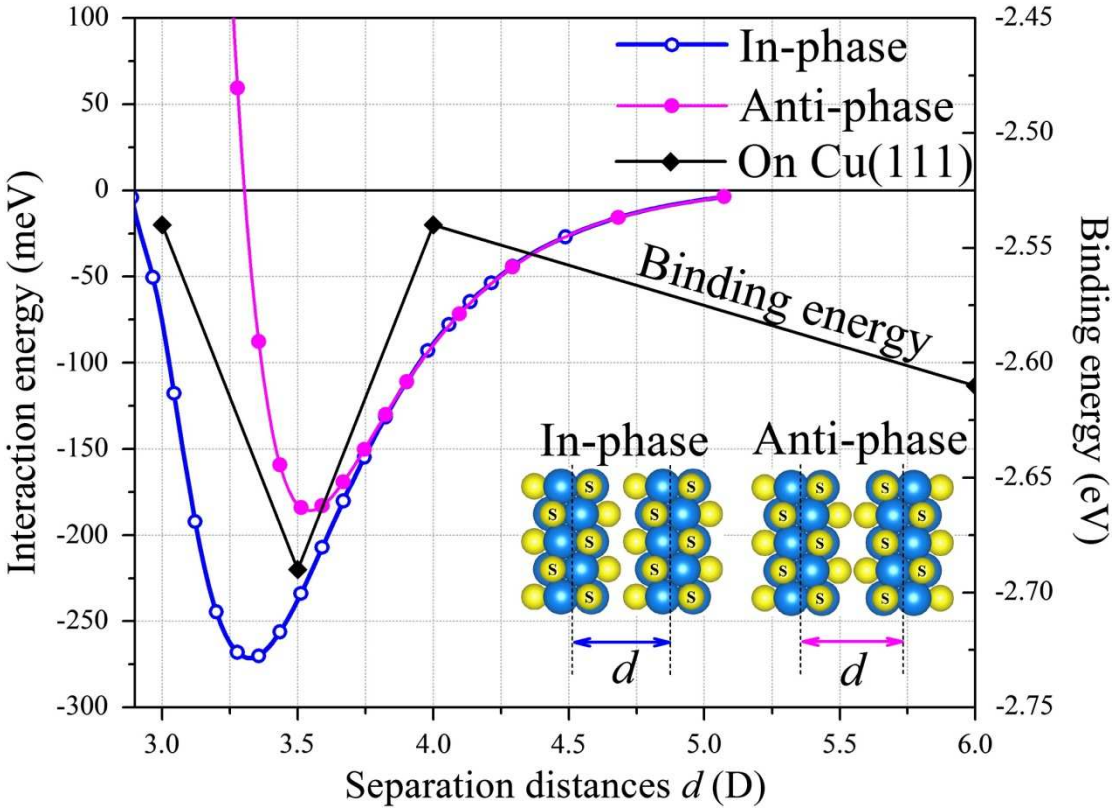

Fig 5.3 Interaction energy between two isolated Mo_6S_6 nanowires per Mo_6S_6 repeat unit (left ordinate) as functions of their separation distance measured in Cu-Cu bond length D. Binding energy of two Mo_6S_6 nanowires to the Cu(111) substrate per Mo_6S_6 repeat unit (right ordinate) as a function of their separation distance. The values are taken for the adsorption configuration (symmetric/asymmetric) that yields optimal binding energy at the indicated separation distances.

On a Cu(111) substrate, the inter-wire distances are limited by substrate registry and cannot be probed continuously in a meaningful manner. On the substrate, the direct vdW interaction of the wires is only one component of the inter-wire interaction:

the presence of the Mo_6S_6 nanowires also causes a significant perturbation of the substrate, which can cause substrate-induced preference for particular interwire distances. At the same time, the presence of the substrate can conceivably screen dispersion interactions. In order to understand whether Mo_6S_6 nanowires have a substrate-controlled preferred separation distance, we modeled wires on Cu(111) at three different separation distances, 3D, 3.5D and 4D using a $\begin{pmatrix} 3 & 3 \\ -1 & 1 \end{pmatrix}$, $\begin{pmatrix} 7 & 7 \\ -1 & 1 \end{pmatrix}$ and $\begin{pmatrix} 4 & 4 \\ -1 & 1 \end{pmatrix}$ or $\begin{pmatrix} 8 & 8 \\ -1 & 1 \end{pmatrix}$ Cu(111) super cell, respectively. We considered both nanowires with symmetric and asymmetric adsorption configurations and arranged them in-phase and in anti-phase configurations, i.e. shifted by 0.5√3D along the wire axis, except for the case of the 3D separation distance, for which the antiphase wires clearly interpenetrate.

Similar substrate-mediated effects have been found for a great number of atomic and molecular adsorbates on Cu(111) and were ascribed largely to the Shockley surface state [121-126]. We note that its theoretical modeling typically requires very thick substrate slabs (8 and more layers) to effectively decouple the surface states on top and on the bottom of the slab [127]. The lateral size of the unit cell required to model nanowire interactions would render such calculations exceedingly time-consuming. Our use of 5 layer slabs limits the quantitative accuracy of our results, yet it reveals the presence of a preferred inter-wire separation distance on the substrate, in-line with our experimental findings: for the separation distance of 3.5D we find a binding energy per Mo_6S_6 unit to the substrate of 2.69 eV, ~ 80 meV stronger than for isolated chains.

Separation distances of the wires of 3D and 4D lead to a binding energy of ~ 2.54 eV, which is weaker than the binding energy of 3.5D separated wires.

Experimentally, we have not optimized the growth of Mo_6S_6 nanowires sufficiently to quantify statistically the interaction energy between adjacent wires. Such measurements have been carried out for interatomic and intermolecular separation distributions [122-124] and permitted mapping of an interwire interaction potential similar to Fig 5.3. In our measurements, however, we observe not only the growth of isolated Mo_6S_6 nanowire as shown in Fig 2a, but also a propensity for their growth in parallel arrays at the 4D separation distance (Fig 5.2c). In contrast, if the nanowires start to grow so that their separation distance is smaller than 4D they terminate to avoid running in parallel (see, for instance, the Mo_6S_6 nanowires at 3D on the left of Fig 5.2b). In combination these findings attest to the presence of interwire interactions that favor a specific separation distance between adjacent nanowires even on a surface.

5.4 Conclusions

We observe the growth of molybdenum–sulfur nanowires on a Cu(111) surface and identify them as Mo_6S_6 nanowires. We find that the substrate interactions are considerable, leading to the alignment of the nanowires with the substrate atomic rows. The nanowire growth favors a 4D separation distance on Cu(111), sufficiently far to separate them completely and slightly wider than expected from DFT simulation. In

combination, our results suggest that Cu(111) may be a viable candidate for the aligned and regularly-spaced growth of Mo_6S_6 nanowires.

Chapter 6 Modification of MoS_x Structures by Inducing Sulfur Defects

The following work is an ongoing project which has not been published. This was collaborative work reporting on measurements by me and other graduate student (C. Wang, D. Sun, Q. Ma). Computational support came from C. Wang at Ludwig Bartels' group at the University of California, Riverside and D. Le at Talat Rahman's group at the University of Central Florida.

6.1 Defects on Mo_2S_3

The finding of a thermally stable molybdenum-sulfur structure(Mo_2S_3) [108] that has higher affinity for adsorbate interaction than the much discussed MoS_2 brims is exciting and suggestive of its relevance to existing catalytic applications, or its utility as an inverse catalyst,[98] yet reactor studies will be necessary to confirm this conclusively. To show that its affinity is not limited to AQ, we also explored the adsorption of an adsorbate pertinent to MoS_x' use as a catalyst in alcohol formation, formic acid (FA), even though its potential for high mobility and its much smaller height signature in STM render the resultant data less straightforward to evaluate. We also attempted to adsorb CO on the MoS_x structures, but could not resolve its image on the surface, probably because at ~25K sample temperature it was moving too rapidly (CO starts diffusing on Cu(111) at ~40K and the passivated surfaces

investigated here offer CO-interactions weaker than those of metallic copper, as shown in our calculations).[128, 129]

In experiments with FA exposure (up to 10 L, under a procedure similar to that employed for AQ) we observe a surface that appears pristinely clean in areas covered by the √7 S-Cu structure or MoS_2 layers (Fig 6.1a), attesting that at these areas the FA will not remain on the sample during annealing to near RT or is so mobile that it is not resolved. Only the Mo_2S_3 surface exhibits an effect of exposure to FA: its corrugation appears checkered (Fig. 6.1b), with three different apparent heights.

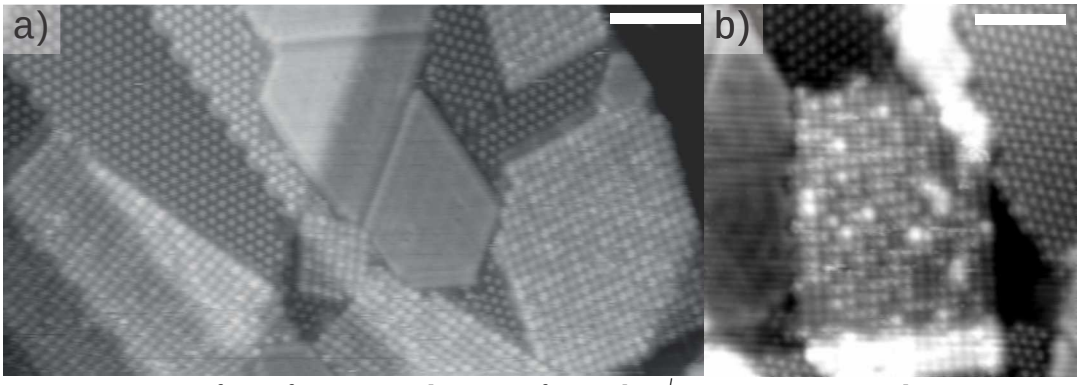

Fig 6.1 STM image of a surface exposed to 10L of FA. The √7 S-Cu structure and MoS_2 are seen to be unperturbed by FA adsorption. Mo_2S_3 patches appear slightly checkered. b) Mo_2S_3 island imaged with a tip particularly sensitive to the three apparent surface heights attributed in the text to adsorption of formate and formic acid. Imaging Parameters (both images): Bias = -0.84V, Current = 0.15nA.

Preliminary modeling of the adsorption of FA on Mo_2S_3 indicate that the adsorption can proceed as formic acid at a binding energy of 2.43 eV or as dissociated species – formate and a hydrogen atom –for a total binding energy of 2.78 eV. Simulation of the STM images shows a very pronounced feature for FA and a less pronounced one for formate, while the abstracted hydrogen atom reduces the

apparent corrugation. Consequently, we interpret Fig 6.1b as showing FA (very prominent) and formate species (less prominent) on the surface and thus as attesting to the ability of the new Mo_2S_3 structure to bind small molecular species and activate hydrogen/proton transfer. Annealing of the surface to >500K restores its original setup (Fig 4.1) and no residue of FA is found.

6.2 Defects on MoS_2

Like graphene, single-layer MoS_2 is stable in air for extended periods of time. In carbon-based materials, such as nanotubes and graphene, this high stability, while attractive for many purposes, has proven a challenge for other needs. Intense processing is required, for example, to bond covalently to these materials, to render them soluble, and to alter their electronic properties, such as by hydrogenation or partial oxidation of graphene. For MoS_2, the inertness of the basal plane calls for interventions to facilitate chemical reactions. In this regard, theoretical studies indicate that sulfur vacancies are reactive. [130]

The work from my group has shown that sputtering with a beam of low-energy argon ions provides a method for selective desulfurization of monolayer MoS_2. The spectroscopic studies and DFT modeling suggest that the basic physical structure of the MoS_2 remains largely intact as the sulfur is removed. Our findings suggest that low-energy argon sputtering may have significant potential for the activation, functionalization, and modification of MoS_2 layers. Although not studied systematically,

the sharp increase in reactivity of the processed MoS_2 monolayer is apparent from its rapid oxidation in air.[131]

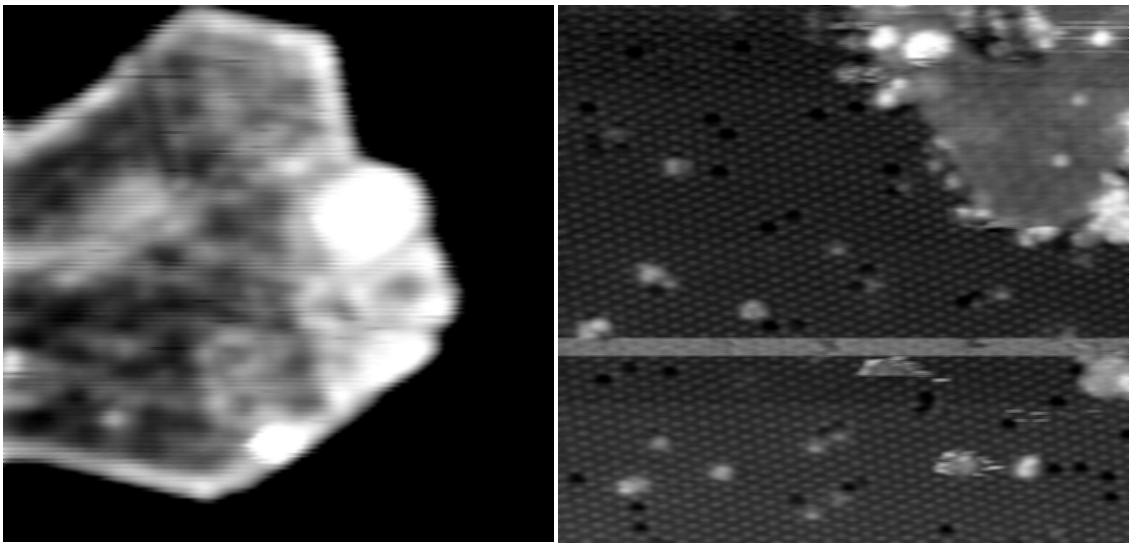

Fig 6.2 STM image of MoS_2 monolayer sputtered with 20mA of filament emission current and 500V electric field and $1x10^{-5}$ torr of Ar gas pressure for 10 seconds. Sulfur defects and dislocation lines can be observed on the left image and the sulfur defects on sulfur terminated copper can also be observed on the right image.

Similarly, a monolayer of MoS_2 on Cu(111) was synthesized on Cu(111) with the preparation methods in Chapter 2. Then MoS_2 defects were first produced with 20mA of filament emission current and accelerated by 500V electric field and $5x10^{-6}$ torr of Ar gas pressure for 3 seconds. However, after this sputtering, little change was observed. Therefore, more sputtering was performed with 20mA of filament emission current and accelerated by 500V electric field and $1x10^{-5}$ torr of Ar gas pressure for 10 seconds. After sputtering, sulfur defects and dislocation lines which are very different from MoS_2 moiré pattern could be observed on the left image of Fig 6.2. The sulfur defects on sulfur terminated copper could also be observed on the right image of Fig 6.2. But the defects

coverage is still not enough and more defects need to be induced by sputtering the sample. The coverage of the defects on MoS_2 can be calibrated by comparing the defects coverage on sulfur terminated copper.

After more defects are prepared on MoS_2, more work about the electronic properties and catalytic properties will be done with our STM system supported with DFT calculations in near future.

Chapter 7 Summary

Summary

STM is a powerful scientific instrument because it can image materials at single atom/molecule level and identify the position of each atom/molecule relative to the substrate. STM can also explore the local density of states and investigate how the local environment (neighbor molecules, local defects, surface mediated forces, geometry of the substrate, etc.) change and tailor the surface electronic setup, which eventually governs the ordering of the whole material. In turn, this determines the material's mechanical and electronic properties.

We found that MoS_2 films of tens of nanometers in size can be grown on Cu(111) at moderate temperatures using thiophenol as an easy to handle sulfur source and molybdenum deposited via e-beam evaporation (physical vapor deposition). Given that electrochemically-prepared copper films are dominantly covered by (111) facets, this process may have potential for application far beyond this single crystal study.

A novel MoS_x surface structure was found to be grown on copper, which we proposed to have the composition Mo_2S_3. Its ability to interact and activate adsorbates far exceeded that of MoS_2, at the same time, the material proved to be of similar thermal stability and also recoverable after adsorption through annealing. Some catalyst compositions of MoS_x for the formation of products from syngas contain copper; thus,

this finding of a high affinity MoSx composition specifically on copper potentially point toward an alternative origin of the actual working of such a catalyst.

We also observed the growth of molybdenum–sulfur nanowires on a Cu(111) surface and identified them as Mo_6S_6 nanowires. We found that the substrate interactions were considerable, leading to the alignment of the nanowires with the substrate atomic rows. The nanowire growth favors a 4D separation distance on Cu(111), sufficiently far to separate them completely and slightly wider than expected from DFT simulation. In combination, this study suggests that Cu(111) may be a viable candidate for the aligned and regularly-spaced growth of Mo_6S_6 nanowires.

Future Work

For the project of MoS_2 defects on Cu(111) substrate, optimizing the growth parameter may lead to large flake formation. Further optimization of sputtering is necessary for inducing enough defects on MoS_2 monolayer.

Based on our experimental result and literatures [131], The work has shown that sputtering with a beam of low-energy argon ions provides a method for selective desulfurization of monolayer MoS_2. The spectroscopic studies and DFT modeling suggest that the basic physical structure of the MoS_2 remains largely intact as the sulfur is removed. Our findings suggest that low-energy argon sputtering may have significant potential for the activation, functionalization, and modification of MoS_2 layers. There are mainly two methods to induce defects on MoS_2 monolayer on Cu(111). One method is to sputter off sulfur atoms to the extent as expected which

may be difficult to control experimentally. The other is to sputter off many more sulfur atoms than expected with a further recovering of sulfur by introducing thiophenal. Both of the methods will be tested for optimizing the defects coverage on MoS_2. Further more work about the electronic properties and catalytic properties will be done with our STM system supported by DFT calculations.

References

[1] C. Kettel, Wiley New York, (1996).

[2] K.Y. Kwon, Disseration, UC, Riverside, Riverside, 2005, pp. 136.

[3] J. Tersoff, D.R. Hamann, Phys Rev B, 31 (1985) 805-813.

[4] D. Kim, D.Z. Sun, W.H. Lu, Z.H. Cheng, Y.M. Zhu, D. Le, T.S. Rahman, L. Bartels, Langmuir, 27 (2011) 11650-11653.

[5] G. Binnig, H. Rohrer, Helv Phys Acta, 55 (1982) 726-735.

[6] M. Baumer, H.J. Freund, Prog Surf Sci, 61 (1999) 127-198.

[7] G. Meyer, L. Bartels, K.H. Rieder, Comp Mater Sci, 20 (2001) 443-450.

[8] W.P. Moore AM, Annu Rev Anal Chem 1(2008) 857-882.

[9] J.H. Tersoff, DR., Phys. Rev. B, 31 (1985) 805–813.

[10] G. N., IBM J. Res. Develop., (1986) 533-542.

[11] J.H. Coombs, M.E. Welland, J.B. Pethica, Surf Sci, 198 (1988) L353-L358.

[12] J. Tersoff, D.R. Hamann, Phys Rev Lett, 50 (1983) 1998-2001.

[13] G. Kresse, J. Hafner, Physical Review B: Condensed Matter and Materials Physics, 47 (1993) 558-561.

[14] J.P. Perdew, Y. Wang, Phys Rev B, 45 (1992) 13244-13249.

[15] M.C. Payne, M.P. Teter, D.C. Allan, T.A. Arias, J.D. Joannopoulos, Reviews of Modern Physics, 64 (1992) 1045-1097.

[16] K.F. Mak, C. Lee, J. Hone, J. Shan, T.F. Heinz, Phys. Rev. Lett., 105 (2010) 136805.

[17] A. Splendiani, L. Sun, Y.B. Zhang, T.S. Li, J. Kim, C.Y. Chim, G. Galli, F. Wang, Nano Lett, 10 (2010) 1271-1275.

[18] B. Radisavljevic, A. Radenovic, J. Brivio, V. Giacometti, A. Kis, Nat Nanotechnol, 6 (2011) 147-150.

[19] R. Tenne, A. Albu-Yaron, M. Levy, R. Popovitz-Biro, M. Weidenbach, M. Bar-Sadan, L. Houben, A.N. Enyashin, G. Seifert, D. Feuermann, E.A. Katz, J.M. Gordon, Angew. Chem. Int. Ed. Engl., 50 (2011) 1810-1814.

[20] C.N.R. Rao, A. Nag, European Journal of Inorganic Chemistry, (2010) 4244-4250.

[21] K.S. Novoselov, D. Jiang, F. Schedin, T.J. Booth, V.V. Khotkevich, S.V. Morozov, A.K. Geim, P Natl Acad Sci USA, 102 (2005) 10451-10453.

[22] J.N. Coleman, M. Lotya, A. O'Neill, S.D. Bergin, P.J. King, U. Khan, K. Young, A. Gaucher, S. De, R.J. Smith, I.V. Shvets, S.K. Arora, G. Stanton, H.Y. Kim, K. Lee, G.T. Kim, G.S. Duesberg, T. Hallam, J.J. Boland, J.J. Wang, J.F. Donegan, J.C. Grunlan, G. Moriarty, A. Shmeliov, R.J. Nicholls, J.M. Perkins, E.M. Grieveson, K. Theuwissen, D.W. McComb, P.D. Nellist, V. Nicolosi, Science, 331 (2011) 568-571.

[23] J.M. Lightstone, M.J. Patterson, P. Liu, J.C. Lofaro, M.G. White, J. Phys. Chem. C, 112 (2008) 11495-11506.

[24] S. Bae, H. Kim, Y. Lee, X.F. Xu, J.S. Park, Y. Zheng, J. Balakrishnan, T. Lei, H.R. Kim, Y.I. Song, Y.J. Kim, K.S. Kim, B. Ozyilmaz, J.H. Ahn, B.H. Hong, S. Iijima, Nat Nanotechnol, 5 (2010) 574-578.

[25] A.T. N'Diaye, S. Bleikamp, P.J. Feibelman, T. Michely, Phys. Rev. Lett., 97 (2006) .

[26] S. Helveg, J. Lauritsen, E. Laegsgaard, I. Stensgaard, J. Norskov, B. Clausen, H. Topsoe, F. Besenbacher, Phys. Rev. Lett., 84 (2000) 951-954.

[27] J.A. Rodriguez, J. Dvorak, T. Jirsak, J. Hrbek, Surf. Sci., 490 (2001) 315-326.

[28] B.J. Hinch, J.W.M. Frenken, G. Zhang, J.P. Toennies, Surf. Sci., 259 (1991) 288-300.

[29] M. Foss, R. Feidenhansl, M. Nielsen, E. Findeisen, T. Buslaps, R.L. Johnson, Surf Sci, 388 (1997) 5-14.

[30] G.J. Jackson, S.M. Driver, D.P. Woodruff, B.C.C. Cowie, R.G. Jones, Surf Sci, 453 (2000) 183-190.

[31] M. May, S. Gonzalez, F. Illas, Surf Sci, 602 (2008) 906-913.

[32] E. Wahlstrom, I. Ekvall, H. Olin, S.A. Lindgren, L. Wallden, PHYSICAL REVIEW B, 60 (1999) 10699.

[33] E. Wahlstrom, I. Ekvall, T. Kihlgren, H. Olin, S.A. Lindgren, L. Wallden, Phys. Rev. B, 64 (2001) 155406.

[34] L. Ruan, I. Stensgaard, F. Besenbacher, E. Laegsgaard, ULTRAMICROSCOPY, 42-44 (1992) 498-504.

[35] K.L. Wong, X. Lin, K.Y. Kwon, G. Pawin, B.V. Rao, A. Liu, L. Bartels, S. Stolbov, T.S. Rahman, Langmuir, 20 (2004) 10928-10934.

[36] K. Berland, T.L. Einstein, P. Hyldgaard, Phys. Rev. B, 80 (2009) 155431.

[37] K. Toyoda, Y. Nakano, I. Hamada, K. Lee, S. Yanagisawa, Y. Morikawa, Surf. Sci., 603 (2009) 2912-2922.

[38] T.A. Patterson, J.C. Carver, D.E. Leyden, D.M. Hercules, J. Phys. Chem., 80 (1976) 1700-1708.

[39] M.A. Baker, R. Gilmore, C. Lenardi, W. Gissler, Appl. Surf. Sci., 150 (1999) 255-262.

[40] A.H. Castro Neto, F. Guinea, N.M.R. Peres, K.S. Novoselov, A.K. Geim, Rev Mod Phys, 81 (2009) 109-162.

[41] Y.Q. Wu, Y.M. Lin, A.A. Bol, K.A. Jenkins, F.N. Xia, D.B. Farmer, Y. Zhu, P. Avouris, Nature, 472 (2011) 74-78.

[42] A. Ayari, E. Cobas, O. Ogundadegbe, M.S. Fuhrer, J Appl Phys, 101 (2007).

[43] K.F. Mak, C. Lee, J. Hone, J. Shan, T.F. Heinz, Phys Rev Lett, 105 (2010).

[44] S. Ghatak, A.N. Pal, A. Ghosh, Acs Nano, 5 (2011) 7707-7712.

[45] Y. Yoon, K. Ganapathi, S. Salahuddin, Nano Lett, 11 (2011) 3768-3773.

[46] W. Moritz, B. Wang, M.L. Bocquet, T. Brugger, T. Greber, J. Wintterlin, S. Gunther, Phys Rev Lett, 104 (2010).

[47] D. Stradi, S. Barja, C. Diaz, M. Garnica, B. Borca, J.J. Hinarejos, D. Sanchez-Portal, M. Alcami, A. Arnau, A.L.V. de Parga, R. Miranda, F. Martin, Phys Rev Lett, 106 (2011).

[48] R. Laskowski, P. Blaha, T. Gallauner, K. Schwarz, Phys Rev Lett, 98 (2007).

[49] M. Dion, H. Rydberg, E. Schroder, D.C. Langreth, B.I. Lundqvist, Phys Rev Lett, 92 (2004).

[50] T. Thonhauser, V.R. Cooper, S. Li, A. Puzder, P. Hyldgaard, D.C. Langreth, Phys Rev B, 76 (2007).

[51] G. Roman-Perez, J.M. Soler, Phys Rev Lett, 103 (2009).

[52] P. Giannozzi, S. Baroni, N. Bonini, M. Calandra, R. Car, C. Cavazzoni, D. Ceresoli, G.L. Chiarotti, M. Cococcioni, I. Dabo, A. Dal Corso, S. de Gironcoli, S. Fabris, G. Fratesi, R. Gebauer, U. Gerstmann, C. Gougoussis, A. Kokalj, M. Lazzeri, L. Martin-Samos, N. Marzari, F. Mauri, R. Mazzarello, S. Paolini, A. Pasquarello, L. Paulatto, C. Sbraccia, S. Scandolo, G. Sclauzero, A.P. Seitsonen, A. Smogunov, P. Umari, R.M. Wentzcovitch, J Phys-Condens Mat, 21 (2009).

[53] Y.K. Zhang, W.T. Yang, Phys Rev Lett, 80 (1998) 890-890.

[54] T. Boker, R. Severin, A. Muller, C. Janowitz, R. Manzke, D. Voss, P. Kruger, A. Mazur, J. Pollmann, Phys Rev B, 64 (2001).

[55] X.Y. Pang, R.P. Ren, L.Q. Xue, G.C. Wang, Acta Phys-Chim Sin, 23 (2007) 1109-1112.

[56] M.V. Bollinger, J.V. Lauritsen, K.W. Jacobsen, J.K. Norskov, S. Helveg, F. Besenbacher, Phys Rev Lett, 87 (2001).

[57] C. Busse, P. Lazic, R. Djemour, J. Coraux, T. Gerber, N. Atodiresei, V. Caciuc, R. Brako, A.T. N'Diaye, S. Blugel, J. Zegenhagen, T. Michely, Phys Rev Lett, 107 (2011).

[58] V.R. Surisetty, A.K. Dalai, J. Kozinski, Appl Catal a-Gen, 393 (2011) 50-58.

[59] C.R.F. Lund, Ind Eng Chem Res, 35 (1996) 3067-3073.

[60] G.Z. Bian, Y.L. Fu, Y.S. Ma, Catal Today, 51 (1999) 187-193.

[61] S. Zaman, K.J. Smith, Catal Rev, 54 (2012) 41-132.

[62] X.G. Li, L.J. Feng, Z.Y. Liu, B. Zhong, D.B. Dadyburjor, E.L. Kugler, Ind Eng Chem Res, 37 (1998) 3853-3863.

[63] L.J. Feng, X.G. Li, D.B. Dadyburjor, E.L. Kugler, J Catal, 190 (2000) 1-13.

[64] X.G. Li, L.J. Feng, L.J. Zhang, D.B. Dadyburjor, E.L. Kugler, Molecules, 8 (2003) 13-30.

[65] Z.B. Chen, J. Kibsgaard, T.F. Jaramillo, P Soc Photo-Opt Ins, 7770 (2010).

[66] S. Helveg, J.V. Lauritsen, E. Laegsgaard, I. Stensgaard, J.K. Norskov, B.S. Clausen, H. Topsoe, F. Besenbacher, Phys Rev Lett, 84 (2000) 951-954.

[67] J. Kibsgaard, J.V. Lauritsen, E. Laegsgaard, B.S. Clausen, H. Topsoe, F. Besenbacher, J Am Chem Soc, 128 (2006) 13950-13958.

[68] J.V. Lauritsen, J. Kibsgaard, S. Helveg, H. Topsoe, B.S. Clausen, E. Laegsgaard, F. Besenbacher, Nat Nanotechnol, 2 (2007) 53-58.

[69] J. Kibsgaard, A. Tuxen, M. Levisen, E. Laegsgaard, S. Gemming, G. Seifert, J.V. Lauritsen, F. Besenbacher, Nano Lett, 8 (2008) 3928-3931.

[70] C. Kisielowski, Q.M. Ramasse, L.P. Hansen, M. Brorson, A. Carlsson, A.M. Molenbroek, H. Topsoe, S. Helveg, Angew Chem Int Edit, 49 (2010) 2708-2710.

[71] L.P. Hansen, Q.M. Ramasse, C. Kisielowski, M. Brorson, E. Johnson, H. Topsoe, S. Helveg, Angew Chem Int Edit, 50 (2011) 10153-10156.

[72] Y.H. Lee, X.Q. Zhang, W.J. Zhang, M.T. Chang, C.T. Lin, K.D. Chang, Y.C. Yu, J.T.W. Wang, C.S. Chang, L.J. Li, T.W. Lin, Adv Mater, 24 (2012) 2320-2325.

[73] K.K. Liu, W.J. Zhang, Y.H. Lee, Y.C. Lin, M.T. Chang, C. Su, C.S. Chang, H. Li, Y.M. Shi, H. Zhang, C.S. Lai, L.J. Li, Nano Lett, 12 (2012) 1538-1544.

[74] P.E. Blochl, Phys Rev B, 50 (1994) 17953-17979.

[75] P.E. Blochl, C.J. Forst, J. Schimpl, B Mater Sci, 26 (2003) 33-41.

[76] J.J. Mortensen, L.B. Hansen, K.W. Jacobsen, Phys Rev B, 71 (2005).

[77] J. Klimes, D.R. Bowler, A. Michaelides, J Phys-Condens Mat, 22 (2010).

[78] F. Mittendorfer, A. Garhofer, J. Redinger, J. Klimes, J. Harl, G. Kresse, Phys Rev B, 84 (2011).

[79] J. Harl, G. Kresse, Phys Rev Lett, 103 (2009).

[80] J.L. Domange, J. Oudar, Surf Sci, 11 (1968) 124.

[81] N.P. Prince, D.L. Seymour, M.J. Ashwin, C.F. Mcconville, D.P. Woodruff, R.G. Jones, Surf Sci, 230 (1990) 13-26.

[82] K. Motai, T. Hashizume, H. Lu, D. Jeon, T. Sakurai, H.W. Pickering, Appl Surf Sci, 67 (1993) 246-251.

[83] M. Saidy, K.A.R. Mitchell, Surf Sci, 441 (1999) 425-435.

[84] E. Wahlstrom, I. Ekvall, T. Kihlgren, H. Olin, S.A. Lindgren, L. Wallden, Phys Rev B, 64 (2001).

[85] D.R. Alfonso, J Phys Chem C, 115 (2011) 17077-17091.

[86] J.V. Lauritsen, M. Nyberg, R.T. Vang, M.V. Bollinger, B.S. Clausen, H. Topsoe, K.W. Jacobsen, E. Laegsgaard, J.K. Norskov, F. Besenbacher, Nanotechnology, 14 (2003) 385-389.

[87] J. Zhang, J.M. Soon, K.P. Loh, J.H. Yin, J. Ding, M.B. Sullivian, P. Wu, Nano Lett, 7 (2007) 2370-2376.

[88] R.K. Tiwari, J.S. Yang, M. Saeys, C. Joachim, Surf Sci, 602 (2008) 2628-2633.

[89] M.L. Tang, D.C. Grauer, B. Lassalle-Kaiser, V.K. Yachandra, L. Amirav, J.R. Long, J. Yano, A.P. Alivisatos, Angew Chem Int Edit, 50 (2011) 10203-10207.

[90] Y.J. Zhang, J.T. Ye, Y. Matsuhashi, Y. Iwasa, Nano Lett, 12 (2012) 1136-1140.

[91] G. Pawin, K.L. Wong, K.Y. Kwon, L. Bartels, Science, 313 (2006) 961-962.

[92] G. Pawin, U. Solanki, K.Y. Kwon, K.L. Wong, X. Lin, T. Jiao, L. Bartels, J Am Chem Soc, 129 (2007) 12056.

[93] K.Y. Kwon, G. Pawin, K.L. Wong, E. Peters, D. Kim, S. Hong, T.S. Rahman, M. Marsella, L. Bartels, J Am Chem Soc, 131 (2009) 5540-5545.

[94] P. Johari, V.B. Shenoy, Acs Nano, 5 (2011) 5903-5908.

[95] A. Ramasubramaniam, D. Naveh, E. Towe, Phys Rev B, 84 (2011).

[96] D. Le, D.Z. Sun, W.H. Lu, L. Bartels, T.S. Rahman, Phys Rev B, 85 (2012).

[97] Q. Yue, J. Kang, Z.Z. Shao, X.A. Zhang, S.L. Chang, G. Wang, S.Q. Qin, J.B. Li, Phys Lett A, 376 (2012) 1166-1170.

[98] J.A. Rodriguez, J. Hrbek, Surf Sci, 604 (2010) 241-244.

[99] A.J. Heinrich, C.P. Lutz, J.A. Gupta, D.M. Eigler, Science, 298 (2002) 1381-1387.

[100] K.-Y. Kwon, University of California, Riverside2005, pp. ix, 136 leaves.

[101] Q.H. Wang, K. Kalantar-Zadeh, A. Kis, J.N. Coleman, M.S. Strano, Nat Nanotechnol, 7 (2012) 699-712.

[102] G. Eda, H. Yamaguchi, D. Voiry, T. Fujita, M.W. Chen, M. Chhowalla, Nano Lett, 11 (2011) 5111-5116.

[103] T. Cao, G. Wang, W.P. Han, H.Q. Ye, C.R. Zhu, J.R. Shi, Q. Niu, P.H. Tan, E. Wang, B.L. Liu, J. Feng, Nat Commun, 3 (2012).

[104] K.F. Mak, K.L. He, J. Shan, T.F. Heinz, Nat Nanotechnol, 7 (2012) 494-498.

[105] G. Sallen, L. Bouet, X. Marie, G. Wang, C.R. Zhu, W.P. Han, Y. Lu, P.H. Tan, T. Amand, B.L. Liu, B. Urbaszek, Phys Rev B, 86 (2012).

[106] D. Xiao, G.B. Liu, W.X. Feng, X.D. Xu, W. Yao, Phys Rev Lett, 108 (2012).

[107] H.L. Zeng, J.F. Dai, W. Yao, D. Xiao, X.D. Cui, Nat Nanotechnol, 7 (2012) 490-493.

[108] D.Z. Sun, W.H. Lu, D. Le, Q. Ma, M. Aminpour, M.A. Ortigoza, S. Bobek, J. Mann, J. Wyrick, T.S. Rahman, L. Bartels, Angew Chem Int Edit, 51 (2012) 10284-10288.

[109] Z.B. Chen, D. Cummins, B.N. Reinecke, E. Clark, M.K. Sunkara, T.F. Jaramillo, Nano Lett, 11 (2011) 4168-4175.

[110] Y.G. Li, H.L. Wang, L.M. Xie, Y.Y. Liang, G.S. Hong, H.J. Dai, J Am Chem Soc, 133 (2011) 7296-7299.

[111] J.D. Benck, Z.B. Chen, L.Y. Kuritzky, A.J. Forman, T.F. Jaramillo, Acs Catal, 2 (2012) 1916-1923.

[112] J. Kibsgaard, Z.B. Chen, B.N. Reinecke, T.F. Jaramillo, Nat Mater, 11 (2012) 963-969.

[113] B. Visic, R. Dominko, M.K. Gunde, N. Hauptman, S.D. Skapin, M. Remskar, Nanoscale Res Lett, 6 (2011) 1-6.

[114] M.A. Albiter, R. Huirache-Acuna, F. Paraguay-Delgado, J.L. Rico, G. Alonso-Nunez, Nanotechnology, 17 (2006) 3473-3481.

[115] I. Wiesel, H. Arbel, A. Albu-Yaron, R. Popovitz-Biro, J.M. Gordon, D. Feuermann, R. Tenne, Nano Res, 2 (2009) 416-424.

[116] X. Zong, Y. Na, F.Y. Wen, G.J. Ma, J.H. Yang, D.G. Wang, Y. Ma, M. Wang, L. Sun, C. Li, Chem Commun, (2009) 4536-4538.

[117] E. DiMasi, V.M. Patel, M. Sivakumar, M.J. Olszta, Y.P. Yang, L.B. Gower, Langmuir, 18 (2002) 8902-8909.

[118] G. Kresse, J. Hafner, Phys Rev B, 48 (1993) 13115-13118.

[119] J. Klimes, D.R. Bowler, A. Michaelides, Phys Rev B, 83 (2011).

[120] J.P. Perdew, K. Burke, M. Ernzerhof, Acs Sym Ser, 629 (1996) 453-462.

[121] G. Binnig, H. Rohrer, C. Gerber, E. Weibel, Phys Rev Lett, 50 (1983) 120-123.

[122] J. Repp, F. Moresco, G. Meyer, K.H. Rieder, P. Hyldgaard, M. Persson, Phys Rev Lett, 85 (2000) 2981-2984.

[123] N. Knorr, H. Brune, M. Epple, A. Hirstein, M.A. Schneider, K. Kern, Phys Rev B, 65 (2002).

[124] T. Mitsui, M.K. Rose, E. Fomin, D.F. Ogletree, M. Salmeron, Phys Rev Lett, 94 (2005).

[125] K.L. Wong, B.V. Rao, G. Pawin, E. Ulin-Avila, L. Bartels, J Chem Phys, 123 (2005).

[126] Y.F. Wang, X. Ge, C. Manzano, J. Korger, R. Berndt, W.A. Hofer, H. Tang, J. Cerda, J Am Chem Soc, 131 (2009) 10400.

[127] I. Lyubinetsky, D.B. Dougherty, T.L. Einstein, E.D. Williams, Phys Rev B, 66 (2002).

[128] K.L. Wong, B.V. Rao, G. Pawin, E. Ulin-Avila, L. Bartels, J. Chem. Phys., 123 (2005) 201102.

[129] A. Heinrich, C. Lutz, J. Gupta, D. Eigler, Science, 298 (2002) 1381-1387.

[130] C. Ataca, S. Ciraci, Phys Rev B, 85 (2012).

[131] Q. Ma, P.M. Odenthal, J. Mann, D. Le, C.S. Wang, Y.M. Zhu, T.Y. Chen, D.Z. Sun, K. Yamaguchi, T. Tran, M. Wurch, J.L. McKinley, J. Wyrick, K. Magnone, T.F. Heinz, T.S. Rahman, R. Kawakami, L. Bartels, J Phys-Condens Mat, 25 (2013).